The Hybrid Mineral Battery: energy storage and dissolution behavior of $CuFeS_2$ in a fixed bed flow cell

K. M. Deen*, E. Asselin

Department of Materials Engineering, The University of British Columbia, Vancouver BC, V6T 1Z4, Canada

*Corresponding Author: kmdeen.ceet@pu.edu.pk, kashif_mairaj83@yahoo.com (K. M. Deen)

Phone: +1–604–782–9397

Abstract

The development of a hybrid system, capable of storing energy, and with the additional benefit of Cu extraction is discussed in this work. A fixed bed flow cell (FBFC) was used in which a composite negative electrode containing $CuFeS_2$ (80 wt. %) and carbon black (20 wt. %) in graphite felt was separated from a positive (graphite felt) electrode by proton exchange membrane. The anolyte (0.2M H_2SO_4) and catholyte (0.5M Fe^{2+} in 0.2M H_2SO_4 with or without 0.1M Cu^{2+} addition) were circulated in the cell. With the addition of Cu^{2+} in the catholyte, the electrochemical activity of the Fe^{2+}/Fe^{3+} redox couple over graphite felt was significantly improved. Ultimately, in the $CuFeS_2||Fe^{2+}/Cu^{2+}$ (CFeCu) FBFC system the specific capacity increased continuously to 26.4 mAh g^{-1} in 500 galvanostatic charge/discharge (GCD) cycles, compared to the $CuFeS_2||Fe^{2+}$ (CFe) system (13.9 mAh g^{-1}). Interestingly, the specific discharge energy gradually increased to 3.6 Wh kg^{-1} in 500 GCD cycles for the CFeCu system compared to 3.29 Wh kg^{-1} for the CFe system in 150 cycles. In addition to the energy storage, 10.75 % Cu was also extracted from the mineral, which is an important feature of CFeCu system as it would allow for Cu extraction and recovery through hydrometallurgical methods.

Keywords: Electrochemistry; Voltammetry; Energy conversion; Interfaces

1. Introduction

Renewable energy sources are always intermittent because of their dependency on geological conditions e.g., weather, time of day or year and location. Therefore, efficient energy storage systems (batteries, supercapacitors etc.) are always required so that they may be used for peak shaving during day and night shifts and could ensure continuous supply on demand [1-7].

Today's rapidly growing population, global warming issues, greenhouse gas emissions and depletion of fossil fuels have also forced researchers to look at alternative ways for metal production. To date, the extractive industries have used minerals mainly for producing metals. However, many minerals possess intrinsic characteristics that could be used for purposes other than metal production e.g. for energy storage. There exists a dichotomy between the current widespread use of these minerals for metal production and their potential application as energy materials. This research work is something radically different: to leverage existing mining infrastructure to rationalize the construction of battery systems and in turn encourage remote locations to build and use renewable energies.

Pyrite (FeS_2) and chalcopyrite ($CuFeS_2$) are well known natural semiconductors that have been studied for use as electrode materials in lithium/sodium ion batteries. Pyrite (FeS_2) is an abundantly available cheap mineral. Primary Li/FeS_2 batteries have already been commercialized in portable electronic devices [8-13]. Chalcopyrite ($CuFeS_2$) is the main economic copper bearing mineral, which is generally processed through pyro-metallurgical methods to extract Cu. But serious environmental issues with smelting, depletion of high grade ores and a large amount of impurities (some toxic) have resulted in continued research aimed at the development of hydrometallurgical technologies. There are a number of different proposed routes in the literature to treat $CuFeS_2$ concentrates, but only a few of them have attained commercial acceptance [14]. The stability of $CuFeS_2$ in aqueous solutions and its tendency to form other phases in oxidizing, reducing, acidic and basic conditions can be explained with an Eh-pH diagram [15]. Several discrepancies related with the difference between theoretical aspects and experimental evidence have been explained in reference [15]. For example, the oxidation of $CuFeS_2$ to Cu_2S (under laboratory conditions) and limited stability of sulfur in acidic and oxidizing conditions are contrary to experimental observations [15, 16].

During acidic oxidative leaching processes, $CuFeS_2$ dissolution is inhibited and this is believed to be one of the main reasons for its slow kinetic response. The nature of this inhibition

(and the passive film that may be responsible) is still controversial and a number of studies describe it as elemental S° [17, 18], disulfide (S_2^{2-}) [19-21], metal deficient poly-sulfides (S_n^{2-}) and/or Fe hydroxy-oxide [22, 23]. However, the mono-sulfide (S^{2-}), disulfide (S_2^{2-}), polysulfide (S_n^{2-}), $Cu_{1-x}Fe_{1-y}S_2$ ($x + y \approx 1$ and $y \gg x$), iron deficient sulfide and CuS_n ($n > 2$) species are detected within the surface film and well documented in the literature [24]. Also, another possible reason of slow $CuFeS_2$ dissolution could be its n–type semi–conductive behaviour as reported by Crundwell and coauthors [25]. They proposed that the slow anodic dissolution of $CuFeS_2$ can be explained by the formation of an electron depletion region at the surface as indicated by the decrease in current due to the application of potential in reverse bias. However, recently, Nicol *et al.* [26] questioned the relevance of the semi-conductive behavior of sulfide minerals i.e. $CuFeS_2$ and FeS_2 during anodic dissolution. It has been proposed that at potentials < 1.0 V, the rate determining step for the dissolution of $CuFeS_2$ was associated with the solid state diffusion of Fe or possibly Cu due to the formation of a less reactive passive film. Also, in direct contradiction to the theory proposed by Crundwell *et al.*, the photocurrent generation during oxidation of these minerals in acidic sulfate solutions was shown by Nicol *et al.* to be related to thermal effects in the semi–conductive surface film and not to the bulk $CuFeS_2$. Despite these contradictions about the mechanism of anodic dissolution of transition metal sulfide minerals, there exists a large consensus on the formation of a metal deficient sulfide sulfur enriched layer at the surface which likely restricts mineral dissolution [27].

Interestingly, the disulfide (S_2^{2-}) species present at the surface of FeS_2 provides a large reversible pseudocapacitance in acidic electrolytes as discovered by Conway *et al.* [28]. In the literature there are a few other useful reports available that describe the augmentation in overall charge storage capacity of high surface area carbon-based electrochemical capacitors after doping with sulfur species [29-32].

The literature provides good insight about the possible leaching of $CuFeS_2$ under oxidizing conditions or by reductive conversion of $CuFeS_2$ into Cu_2S, which could be oxidized easily into Cu^{2+}. The use of Fe^{3+} ions in the presence of oxygen to leach Cu^{2+} from $CuFeS_2$ has been rigorously studied in the past [33–36]. The energy generated at the surface of $CuFeS_2$ during oxidation by Fe^{3+} ions in the presence of oxygen is lost as heat. In contrast to the direct reduction of Fe^{3+} on $CuFeS_2$, we propose that the Fe^{2+}/Fe^{3+} redox reaction could proceed on a separate electrode in a battery like

cell setup. Thus, the amount of useful energy, which may be retrieved and stored for further use, can be quantified.

In this research, the preliminary steps toward the development of a hybrid mineral battery-like system are presented. This device can be used simultaneously as an energy storage device and a unit for metal extraction. Initially, the synthetic $CuFeS_2$ is used as an active anode material due to its unique ability to reduce or oxidize under different conditions, a characteristic that motivated this work. This hybrid setup consists of two simple electrodes in a fixed bed flow cell (FBFC) configuration. The synthetic $CuFeS_2$ mixed with carbon black was sandwiched in graphite felt and this assemblage was used as the negative electrode in which acidic solution was pumped from an external circuit. In the positive half of the cell, the acidic ferrous (*Fe(II))* sulfate solution was circulated through graphite felt, and separated by a proton exchange membrane (PEM) from the other compartment. During charging, the oxidation of Fe^{2+} is expected to reduce $CuFeS_2$ into Cu_2S. In the subsequent discharge cycle, the reduction of Fe^{3+} to Fe^{2+} is anticipated, which facilitates the oxidation of Cu_2S to CuS/Cu^{2+}. Both electrodes were also characterized individually, in their respective electrolytes, to elucidate their electrochemical performance in the final FBFC.

2. Results and Discussion

2.1 Physical characterization of as synthesized $CuFeS_2$

The as synthesized $CuFeS_2$ powder particles were examined by SEM and the formation of pure $CuFeS_2$ was confirmed by X-ray diffraction. Variable size open-pored and platelet-like spherical particles were formed during the hydrothermal synthesis process as shown in Figure 1a. The open pores and thin platelet like morphology could form during the synthesis process by the thermal decomposition of the reagents under high temperature and pressure conditions. Figure 1b shows the diffraction pattern of as synthesized $CuFeS_2$ particles, which matches well with the PDF 37–0471 reference pattern peaks and without presenting any impurity signatures. This also validated the formation of a pure $CuFeS_2$ phase having a tetragonal crystal structure (a, b = 5.289; c = 10.423 A°) and belonging to the I-42d (122) space group. The characteristic peaks observed at 29.3°, 33.8°, 34.4°, 48.7°, 49.0°, 57.8°, 58.5°, 71.2°, 78.8° and 79.4° are indexed, corresponding to the (112), (200), (004), (220), (204), (312), (116), (400), (332) and (316) lattice planes, respectively. Laser particle diffraction of the as–synthesized $CuFeS_2$ showed a wide particle size distribution in the range of ~3 – 45 µm. However, from the cumulative distribution curve, it was

determined that 80 vol. % of the particles (D80) were below ~23.5 ± 2.0 µm as reported in our previous publication [37].

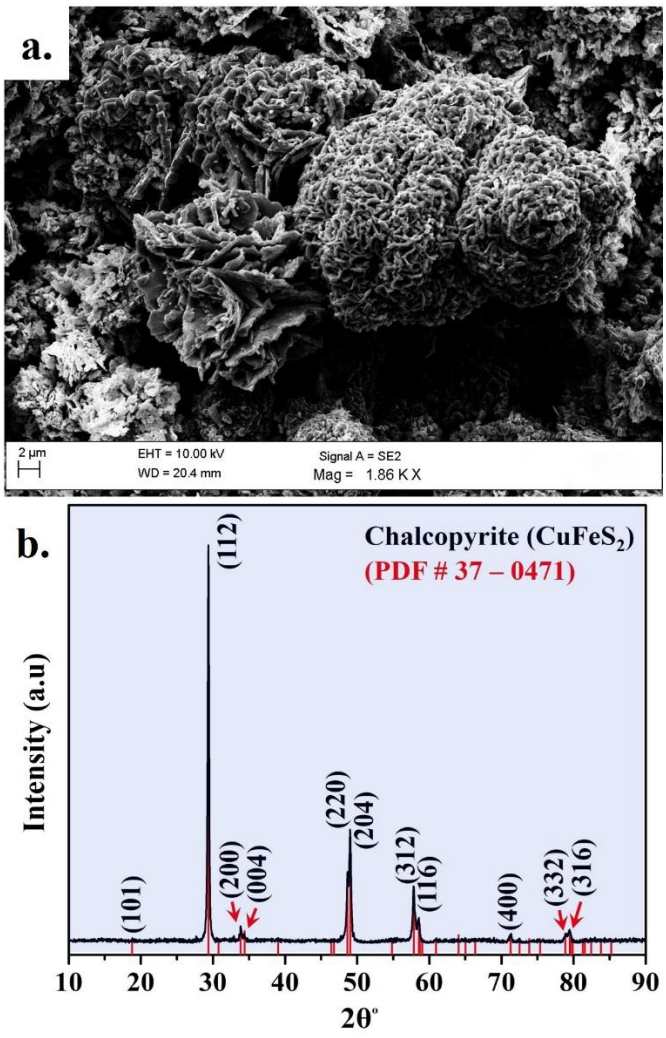

Figure 1: *(a) The morphology of as–synthesized chalcopyrite ($CuFeS_2$) particles (b) XRD pattern showing the pure $CuFeS_2$ phase according to PDF # 37–0471 reference pattern*

The surface area, pore size distribution and pore volume of as–synthesized $CuFeS_2$ particles was determined from the nitrogen adsorption/desorption isotherm obtained at 77 K as shown in Figure S3.The inset shows the magnified region of the isotherm hysteresis observed at large relative pressure ($0.8 < P/P_o < 0.97$) which could be associated with the mesoporous and macro-porous platelet like open structure of spherical $CuFeS_2$ particles. The BET surface area of the $CuFeS_2$ particles (3.5 $m^2\ g^{-1}$) was calculated from the linear portion of the isotherm ($0.05 < P/Po < 0.35$) by the multipoint BET method as only a monolayer of adsorbate (N_2 molecules) is assumed to be formed on the surface of adsorbent within this low relative pressure range [38]. The

surface area is related to the particle size, morphology, pore size and distribution. DFT was employed to evaluate the pore size distribution in the as–synthesized $CuFeS_2$ particles. In the DFT method it was assumed that the pore filling takes place by either micro-pore filling or through capillary condensation. The pores of different sizes are considered to be of regular shape (cylindrical or slit) and the adsorbent surface is assumed to be homogeneous [39]. It was found that the variable sized-pores (5 – 25 nm) were distributed within the $CuFeS_2$ particles and the total pore volume was calculated to be 0.011 $cm^3\ g^{-1}$.

To analyze the surface chemistry of as synthesized $CuFeS_2$, the positive (Figure 2a, b) and negative (Figure 2c, d) ToF-SIMS mass (m/z) spectra were obtained. The positive ion mapping showed Cu enrichment at the surface with relatively small Fe (blue area) concentrations. The mass spectra also provided a Cu/Fe ratio of 1.88, calculated from the corresponding normalized peak intensity. The characteristic peaks for Cu and Fe are shown in Figure 2b with some signals related to the hydrocarbon (HC) impurities [40]. The presence of HCs in the positive spectrum may be due to airborne moieties in the ambient environment during sampling and/or, most likely, to the decomposition products of mineral oil in the vacuum system, which could attach-to and contaminate the sample. The negative ion mapping (Figure 2c) clearly identified the presence of sulfur species at the surface. The mass spectrum of $CuFeS_2$ particles also provided prominent signals for O^-, S^- and HS^- species, as shown in Figure 2d. The significantly higher intensity of O^- in the spectrum could be associated with the oxidation of the surface during exposure to air. However, the larger signals associated with the Cu and S (mostly ionic in nature as elemental sulfur is volatile under ultrahigh vacuum conditions) species at the surface were evident in both positive and negative ion mapping, respectively, which suggest the presence of Cu_x–S_z enriched species at the surface of the $CuFeS_2$ particles. These species may form during synthesis, washing, drying and/or the handling process. Buckley *et al.* [41] also explained the possibility for the formation of iron deficient CuS_2 and $Cu_{0.8}S_2$ species on the surface of $CuFeS_2$ upon exposure to air and during conditioning in acidic solutions, respectively. During exposure to air, a reconstruction process could occur on the fresh surface of $CuFeS_2$ implying that migration of Fe to the surface and reduction of Fe^{3+} would lead to the formation of thin layer enriched with oxide and $Cu_{1-x}S_{2-x}$ ($0 < x \leq 1$) species as discussed by Li *et al.* [42]. This proposed mechanism agrees with the ToF–SIMS and XPS results presented in this study, which also revealed the formation of an Fe deficient, CuS_2 layer on the as–synthesized $CuFeS_2$ particles.

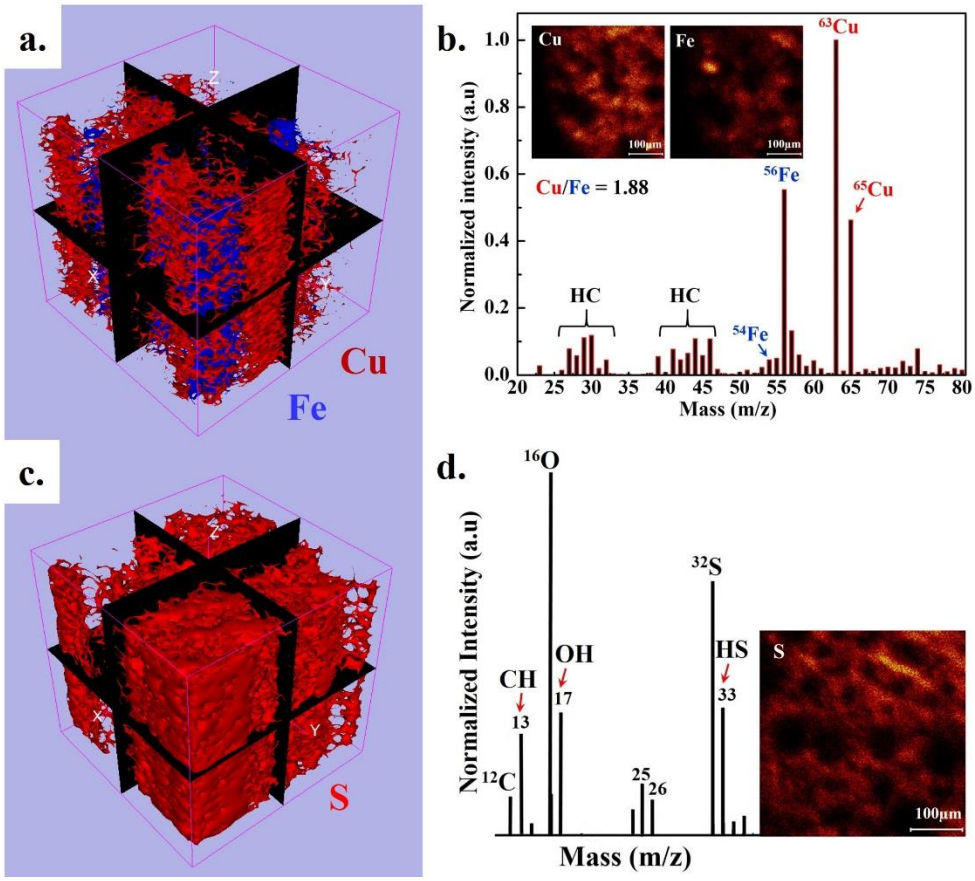

Figure 2: *ToF–SIMS analysis of as synthesized $CuFeS_2$ (a) 3D surface mapping showing the Fe and Cu distribution (b) positive ion mass spectrum representing the composition of surface film (c) 3D mapping for sulfur (S) in the surface film (d) negative ion mass spectrum for surface species identification*

2.2 Electrochemical behavior of individual electrode systems

Both the cathodic and anodic potentiodynamic polarization curves for the composite electrode were obtained at 1 mV s^{-1} scan rate after achieving stability of the OCP (0.01 mV s^{-1}) at 25 ºC, as shown in Figure 3. The cathodic and anodic polarization responses were measured separately on freshly prepared composite electrodes to avoid any effect the conversion products may have had on the polarization scan. The OCP of the composite electrode in 0.2M H_2SO_4 solution was measured to be 0.485 ± 0.01 V, which stabilized after three hours of immersion. The anodic and cathodic Tafel slopes (β_a and β_c) (measured within linear Tafel region but beyond OCP > 50 mV) were 0.202 and 0.303 V/decade corresponding to the charge transfer coefficients 0.29 and 0.19, respectively. Olvera *et al.* [43] also reported similar charge transfer values (α_a = 0.28 and α_c = 0.17 – 0.22) for $CuFeS_2$ in 0.5M H_2SO_4 solution containing ferric and ferrous at 25 ºC. A possible reason for the larger β_a and β_c (low charge transfer coefficients < 0.5) could be the

formation of intermediate species at the surface of $CuFeS_2$ and preferential adsorption of H^o at GF, respectively. However, the open porous structure of GF and the micro porosity of $CuFeS_2$ may also distort the polarization curves, which may result in larger Tafel slopes and lower transfer coefficients, as discussed in the literature [40]. Also at large overpotentials (> ± 0.2 V), the effect of an increase in solution resistance within the porous structure of the composite electrode cannot be neglected.

Three polarization regimes can be observed for the anodic scan in Figure 3. In the low potential range (OCP ≤ E < 0.65 V) (1a), the relatively rapid increase in current is associated with the formation of non-stoichiometric metal deficient polysulfide ($Cu_{1-x}Fe_{1-y}S_2$) at the surface of $CuFeS_2$ via reaction 1 as proposed by other researchers [45-46]. This polysulfide film may restrict further dissolution of $CuFeS_2$ as indicated by the very small increase in anodic current within the (0.65 < E < 1.05 V) potential region (2a).

$$CuFeS_2 \rightarrow Cu_{1-x}Fe_{1-y}S_2 + xCu^{2+} + yFe^{2+} + 2(x + y)\, e^- \quad (y>x) \qquad .1$$

A further increase in potential leads to the transformation of this polysulfide film into CuS_x due to preferred dissolution of iron over copper and with the enrichment of sulfide sulfur at the surface of $CuFeS_2$ [47]. The stability of this polysulfide passive film is reduced at potentials above 1.05 V as indicated by the large increase in the current density (in region 3a). Ghahremaninezhad *et al*. [23] proposed that beyond this potential, the Fe is preferentially released and the dissolution rate of $CuFeS_2$ is further controlled by the copper enriched polysulfide film.

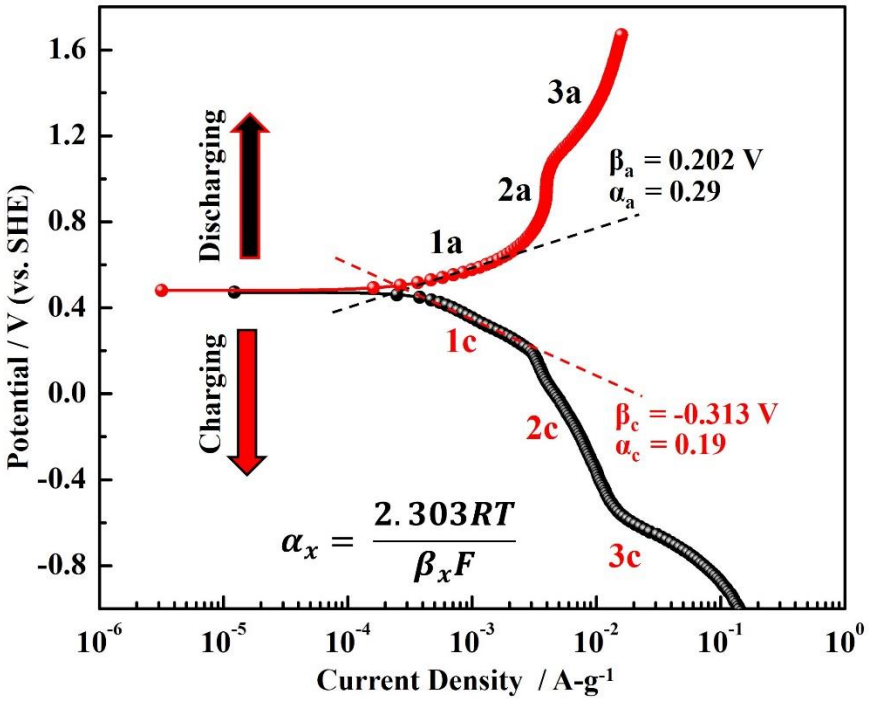

***Figure 3**: Potentiodynamic anodic and cathodic polarization scans of CF – $CuFeS_2$ + CB (composite electrode) in 0.2M H_2SO_4 solution (Note: The current is normalized with the weight of $CuFeS_2$ used to prepare the electrode)*

Cathodic polarization of a separate electrode also resulted in three potential regions. The relatively linear increase in current with shift in potential (OCP > E > 0.18 V) was followed by relatively large polarization effects within (0.2 > E > –0.5 V). This behavior is possibly related to the preferential under potential deposition of H^+ ions at the GF surface, followed by transport to the $CuFeS_2$ within the composite electrode at more negative potentials. The electro-assisted reductive conversion of $CuFeS_2$ into less refractory Cu_2S by monoatomic hydrogen species has also been studied in an undivided cell by Fuentes-Aceituno *et al.* [48]. In the composite electrode, the internal mediator character of GF to generate H^o species and possible reduction of $CuFeS_2$ has been experimentally evaluated in our previous work [37]. Also, it has been discussed in the literature that atomic hydrogen was mobile in graphite and can diffuse along graphene planes at room temperature [49]. Details on the electrochemical reduction of $CuFeS_2$ and formation of intermediate species i.e. talnakhite ($Cu_9Fe_8S_{16}$) and bornite (Cu_5FeS_4) before conversion into chalcocite (Cu_2S) have been given by Nava *et al.* [50].

In the two-electrode cell setup, during charging, the reduction of $CuFeS_2$ (at the negative electrode; GF – $CuFeS_2$) is facilitated by the oxidation of Fe^{2+} into Fe^{3+} on the positive electrode

(GF – Fe). It is therefore important to study the electrochemical behavior of the individual electrode system and to explore the kinetic behavior of any possible faradaic redox reactions that may increase the charge storage capacity in the proposed FBFC system. The influence of 0.1 M Cu^{2+} in 0.5 M Fe^{2+} solution (catholyte) has also been investigated and this refered to as the GF – Fe/Cu electrode system. The CV curves of these electrodes were obtained at various sweep rates and are superimposed to verify the kinetic response as shown in Figure 4. In order to simulate the actual conditions in the final setup, the CV scan for the GF – $CuFeS_2$ (negative electrode) was initiated in the reverse direction before scanning in the positive (forward) direction. It can be seen that the rapid increase in the current density beyond –0.4 V and 1 V both in the reverse and forward directions, respectively, is associated with the dissociation of the electrolyte. Independent of the sweep rate, the most dominant cathodic and anodic peaks were centered at ~0.50 V vs SHE for the GF–$CuFeS_2$ composite electrode system. Both cathodic and anodic peaks were composed of two separate peaks indicating the faradaic response of the surface functional groups present on the GF (indicated as Pc1 and Pa1) and to the reversible character of the sulfide surface species (i.e. polysulfide) present on the $CuFeS_2$ (Pc2 and Pa2) as shown in Figure 4a. With increase in sweep rate, a shift in cathodic peak potentials (Epc1and Epc2) and anodic peak potentials (Epa1 and Epa2) in both negative and positive directions, respectively, was observed. This is most likely associated with the quasi-reversible nature of the redox reactions. However, the solution resistance may also increase within the porous structure during reversible cathodic and anodic scans due to the development of a depletion region that could influence the peak separation. Due to the overlapping current response (broad peaks) by the faradaic reactions affiliated with the surface functional groups and sulfide species (i.e. S_2^{2-}, S^{2-}) at similar potentials (from –0.2 V to 0.7 V vs. SHE), it is difficult to distinguish the individual contributions from the GF and $CuFeS_2$[51–54]. But it is shown in Figure 4d that peak currents (Pa1 and Pc1) vary directly with $v^{1/2}$, corroborating the occurrence of facile reversible electron transfer (capacitive; faradaic) reactions at the electrode leading to a diffusion controlled process. During the cathodic scan, the reduction of $CuFeS_2$ into talnakhite ($Cu_9Fe_8S_{16}$), bornite (Cu_5FeS_4) and chalcocite (Cu_2S) is also possible. At more negative potentials (< –0.1 V), iron is completely removed and the formation of Cu_2S occurs with H_2S generation according to reaction 2.

$$2CuFeS_2 + 6H^+ + 2e^- \rightarrow Cu_2S + 2Fe^{2+} + 3H_2S \quad .2$$

$$CuFeS_2 + 4H^+ + 2e^- \rightarrow Cu + Fe^{2+} + 2H_2S \quad .3$$

For further decrease in potential beyond –0.4 V the formation of metallic copper (reaction 3) in addition to H_2 evolution is also expected. The small but relatively sharp peak at –0.15 V observed during the forward scan could either be associated with the oxidation of metallic copper into Cu^{2+} ions or to the formation of chalcocite as given in reaction 4. The relatively minor peaks observed (from –0.2 V to +0.6 V) during the anodic potential sweep were related to the oxidation of the intermediate species (reaction 5, 6) formed during the reduction reactions [54, 55]. These results corroborate the potentiodynamic polarization behavior as discussed in the previous section.

$$2Cu + H_2S \rightarrow Cu_2S + 2H^+ + 2e^- \quad .4$$

$$Cu_2S \rightarrow Cu_{2-x}S + xCu^{2+} + 2xe^- \quad .5$$

$$H_2S \rightarrow S^o + 2H^+ + 2e^- \quad .6$$

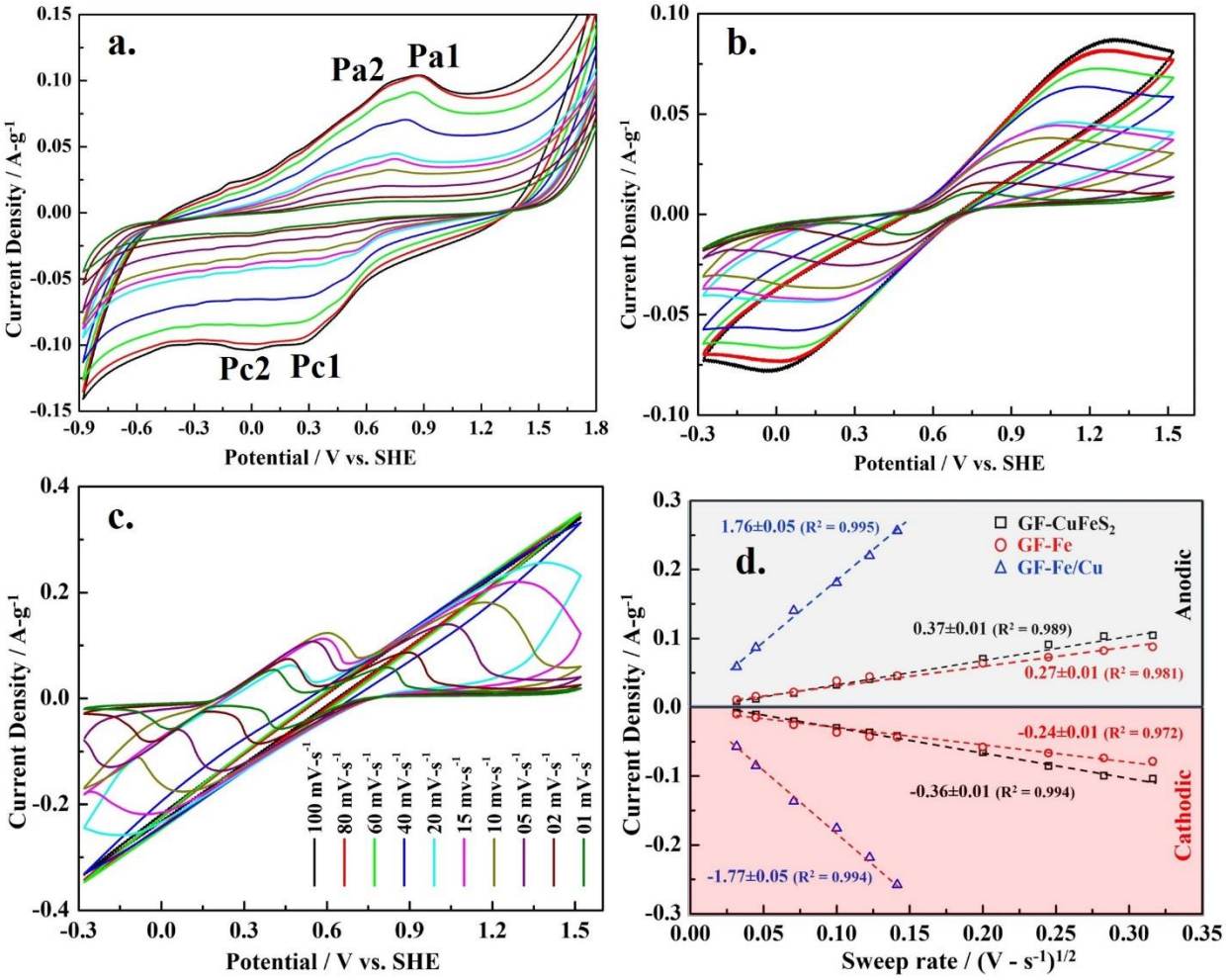

***Figure 4**: Cyclic voltammograms obtained at different sweep rates (a) composite electrode in 0.2 M H_2SO_4 (the current was normalized by the weight of composite electrode) (b) CV of GF electrode in 0.5 M Fe^{2+}+0.2 M H_2SO_4 solution (c) CV of GF in the same solution as in 0.5 M Fe^{2+} + 0.2 M*

H_2SO_4 solution but with the addition of 0.1M Cu^{2+} (The current is normalized by the wt. of GF) (d) The trends of current density vs. (sweep rate)$^{1/2}$ obtained from the CV scans of each electrode

The anodic and cathodic peaks in Figure 4b and 4c correspond to pseudocapacitive Fe^{2+}/Fe^{3+} and $Cu^{2+}/Cu^{+}_{ads,\ GF}$ redox reactions taking place on the GF electrode surface. Thermodynamically, in sulfate media, Cu^{+} in the bulk solution is not stable but it is thought that this intermediate species can form at the surface of GF during reduction of Cu^{2+}. This species may form complexes with the surface functional groups i.e. carbonyl and/carboxylic present on the GF as identified in the IR spectra and reported in the supplementary information of ref. [37]. These redox reactions were further studied from the anodic and cathodic current peak dependency on the sweep rate in the voltammograms. However, the significant distortion in the voltammograms at higher sweep rates, i.e. the shift in both anodic and cathodic peak potentials toward more positive and negative potential values, respectively, was related to the hindered electron transfer processes at the electrode. This behavior could be associated with an increase in solution resistance within the porous structure of GF during forward and reverse scanning. The additional peak in Figure 4c, seen at relatively lower sweep rates (<10 mV s^{-1}), corresponds to the $Cu^{2+}/Cu^{+}_{ads,\ CF}$ couple. The typical behavior of increase in peak current density with square root of sweep rate (figure 4d) corresponds to the faradaic but diffusion controlled electrochemical processes at the GF surface. The peak current for the reverse scan was calculated by subtracting the background current [56] from the baseline produced by Echem Analyst software 6.3 (Gamry Instruments). The pseudocapacitive redox reactions for the Fe^{2+}/Fe^{3+} couple with and without the presence of Cu^{2+} may occur both at the surface and within the porous structure of the GF. This may lead to diffusion controlled kinetic reactions due to the depletion of ionic species within the porous structure of GF and may be validated from the linear dependency of both the anodic and cathodic peak currents on $v^{1/2}$ as shown in Figure 4d.

The GF–Fe/Cu electrode exhibited relatively larger slopes (peak current vs. $v^{1/2}$) (1.76 ± 0.05) (similar for both anodic and cathodic processes) compared to the GF–Fe electrode. This is attributed to the rapid kinetics of the Fe^{2+}/Fe^{3+} redox reaction at the GF electrode in the presence of Cu^{2+}. The redox potential for the Fe^{2+}/Fe^{3+}couple was calculated to be 0.63 ± 0.03 V and the addition of 0.1 M Cu^{2+} did not influence this potential significantly. However, the addition of Cu^{2+} to the electrolyte resulted in an additional peak in the CV scans (Figure 4c), associated with the $Cu^{2+}/Cu^{+}_{ads,\ GF}$ redox reaction. This species also increased the anodic and cathodic peak current

density for the Fe^{2+}/Fe^{3+} couple (at slow sweep rates) compared to the GF–Fe electrode. This behavior indicates an increase in the stability of Fe(III) obtained through the addition of Cu^{2+} in the solution according to reaction 7. However, the effect of increased ionic strength with the addition of Cu^{2+} to the electrolyte cannot be neglected either and further experiments are discussed below to rule this out. The $Cu^{+}_{ads,\ GF}$ species would form as an intermediate species before reduction to metallic 'Cu' and may adsorb by interacting with the surface functional groups present at the surface of GF. This explains the higher discharge current (reduction of Fe^{3+}) for this electrode system.

$$Fe^{2+} + Cu^{2+} \leftrightarrow Fe^{3+} + Cu^{+}_{ads,\ GF} \quad .7$$

To validate the catalytic effect of Cu^{2+} on Fe^{2+} oxidation, step-wise linear sweep voltammetry (LSV) was applied on the GF electrode at 5 mV s^{-1}, as shown in Figure S4. For more information on the experimental procedure and a detailed discussion the reader is advised to see the *supplementary information* attached with this article. It can be inferred from these experimental results (*Figure S4d*) that the addition of Cu^{2+} ions increased the cathodic current for Fe^{3+} reduction, which is directly related to its high concentration and availability at the surface of GF even after a 60 min delay (between charging and discharging). In comparison, the GF–Fe system registered low peak current and validated the beneficial effect of Cu^{2+} addition in the electrolyte. As noted above, this is considered to occur due to the extended stability of Fe^{3+} ions in the solution and catalytic oxidation of Fe^{2+} in the presence of Cu^{2+} ions. However, the addition of 0.5M Fe^{2+} in both electrolytes demonstrated that the increase in current for the Fe^{3+} reduction peaks cannot be related to the increased ionic strength of the solution.

The impedance spectra for the GF–$CuFeS_2$, GF–Fe and GF–Fe/Cu electrode systems were obtained by applying a 5 mV AC potential amplitude over OCP within the frequency range of 10 mHz –100 kHz, as shown in Figure 5 (Nyquist plots) and Figure S5 (Bode plots). The impedance at high frequency is associated with the solution resistance (R_s) and with the charge accumulated in the double layer, which is represented by the constant phase element (Q_{dl}). A constant phase element is used to account for the non–uniform charge distribution within the porous structure of the electrodes. The intermediate and low frequency regimes correspond to the reversible faradaic response of the electrodes, which is inversely related to the charge transfer resistance (R_{ct}). These faradaic reactions (pseudo–capacitive behavior) incorporate specific adsorption of ionic species at the electrode surface (Q_{ad}). In a physical system, the ionic species in the electrolyte (H^+, HSO_4^-,

Fe^{2+} etc.) may interact with the $CuFeS_2$ (in the composite electrode) and/or with the surface functional groups present on the GF [37, 58]. In the EEC model, the parallel resistor (R_{ad}) is used to model the barrier to charge transfer for the adsorption/desorption process. The significant difference in the impedance behavior of the composite and GF electrodes at low frequency can be clearly seen in Figure S5a and S5b. For the composite electrode, the continuous increase in $-Z_{im}$ (at low frequency) is associated with the concentration gradient within the porous structure and to the pre–existing sulfide sulfur enriched species present on the $CuFeS_2$ particles (as confirmed from the ToF–SIMS and XPS analyses, Figure 2 and 10a). This behavior is attributed to the limited mass transport across this film (finite length diffusion) and is modeled by a Warburg coefficient (σ_B) and a time constant (B) in the EEC. However, both GF–Fe and GF–Fe/Cu electrodes had similar trends in the low frequency regime with a slight variation in the phase angle (Figure S5b). This behavior is most likely associated with the semi–infinite diffusion characteristics (σ_w) of the open porous structure of GF.

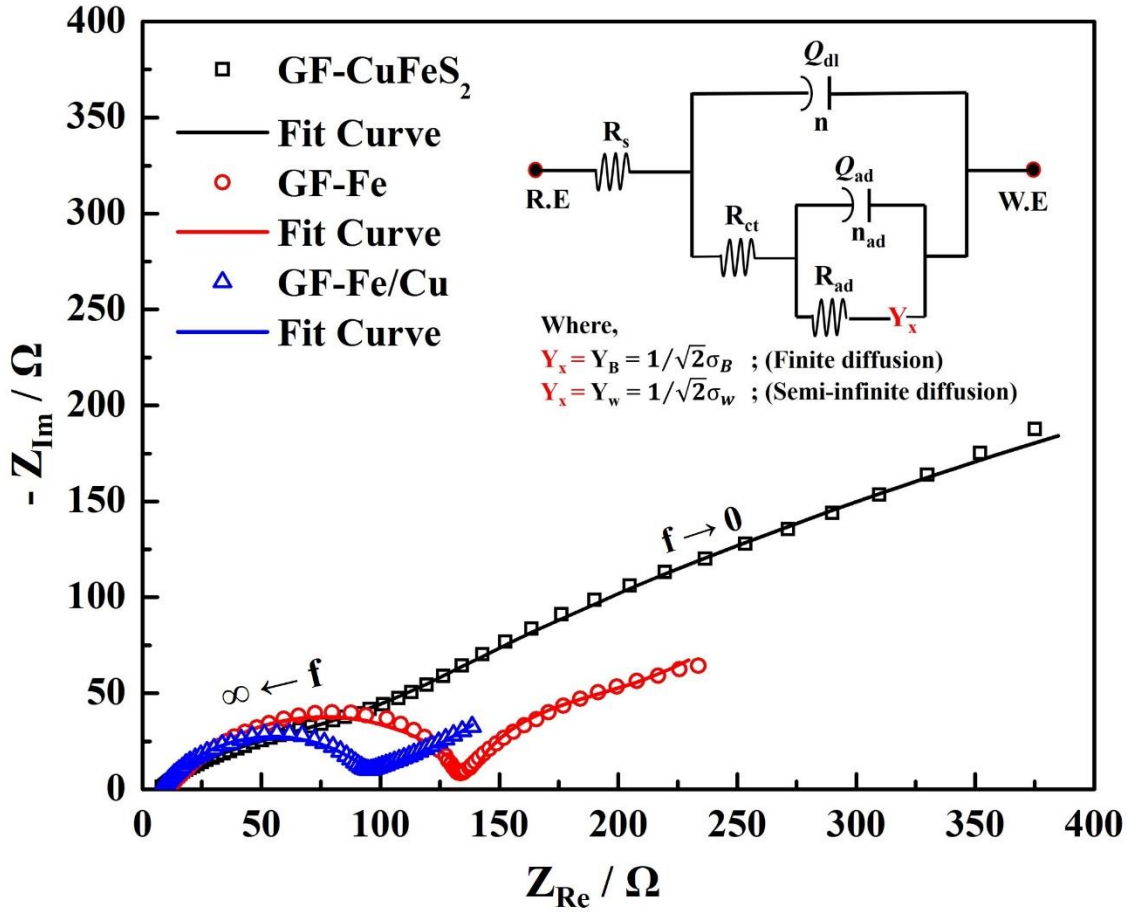

Figure 5: *Impedance spectra of composite (GF – $CuFeS_2$ + CB), GF–Fe and GF–Fe/Cu electrodes measured in their respective electrolytes at 0V vs. OCP DC bias potential, the inset is showing the equivalent electrical circuit model (EEC) used to simulate and fit the experimental results. (Note: Where Y_x is the admittance parameter for the diffusion and x=B, in case of finite diffusion and x=w when there is semi-infinite diffusion, similarly σ_B = Warburg constant for GF–$CuFeS_2$, and σ_w = Warburg constant for GF–Fe and GF–Fe/Cu electrodes. Also, the geometrical area of the GF in all electrodes was same, 14.4 cm^2)*

The data obtained after fitting the EEC model to the impedance spectra is provided in Table S2 (*supplementary information*). The fitting was carried out through an iterative process and by adjusting the parameters of elements in the model editor (Echem Analyst 6.25 software; Gamry Instruments Inc.). The experimental and model values after fitting the EEC had small residual errors as shown in Figure S5c. Compared to GF electrodes, the large 'Q_{dl}' (1.12 mS s^{n1}) registered by the composite electrode is most likely associated with the presence of $CuFeS_2$ in the composite electrode. The sulfide sulfur species (see Figure 10a) on the surface of $CuFeS_2$ and surface functional groups on GF can reversibly interact with ionic species resulting in an increase in 'Q_{dl}'. The kinetic activity (faradaic response) of the composite electrode can be estimated from 'R_{ct}' (84.74 Ω) and is comparable to the GF–Fe/Cu (93.11 Ω) electrode. The higher 'R_{ct}' of GF–Fe (130.2 Ω) compared to GF–Fe/Cu further validated the catalytic behavior of Cu^{2+} in the catholyte as indicated by the improved current response by this electrode (Figures 4c, 4d and *S4*). The reversible faradaic response of the surface sulfide sulfur species and surface functional groups in the composite electrode is reflected by the low 'R_{ad}' (22.34 Ω) value. The small values of 'Q_{ad}' and power index (n_2 = 0.39) are due to a highly distributed faradaic response of the composite electrode [50]. However, limited mass transport across the pre–existing surface film could restrict the non–capacitive faradaic (irreversible) reactions under applied conditions (5 mV AC perturbation at OCP). This behavior can be estimated from the 'σ_B' (606.4 Ω $s^{-1/2}$) and 'B' (1.99 $s^{1/2}$). The relatively large capacitive response 'Q_{dl}' by the GF–Fe/Cu (330.5 µS s^{n1}) compared to GF–Fe (93.9 µS s^{n1}) clearly demonstrated the influence of Cu^{2+} ions in the electrolyte. Due to the porous structure of GF, the non–uniform charge distribution in both electrodes was predicted from $n_1 < 1$ and is evident in the phase shift at high frequency (Figure S5b). The almost double 'Q_{ad}' value (54.9 mS s^{n2}) and very small 'R_{ad}' (16.92 Ω) for the GF–Fe/Cu compared to the GF–Fe electrode further validated the improved kinetic response of the GF in the presence of Cu^{2+} in the electrolyte. The n_2 value equal to 1 indicated the distributed pseudo–capacitive behavior of the porous GF electrode as discussed by Cuenca *et al.* [50]. From these results it can be evaluated that

the reduction of Cu^{2+} at the GF/electrolyte interface (reaction 7) could significantly improve the charge transport characteristics of the GF [58]. On the other hand, the significantly reduced 'σ_w' (7.6 Ω $s^{-1/2}$) for the GF–Fe/Cu electrode compared to GF–Fe electrode is also due to the facile charge transfer process (reaction 7) leading to mass transfer control (semi–infinite diffusion characteristics).

In order to verify this behavior, we immersed the as-received GF samples in each electrolyte for 48 h at 25 °C. The samples were washed with DI–water several times and left in air to dry. The SEM images and EDX analyses of these soaked GF samples showed clear morphological and compositional differences as shown in Figure S6. Compared to the as–received GF and GF–Fe, the GF–Fe/Cu contained higher Fe concentrations. Similarly, the signals for O and S species on the GF–Fe/Cu electrode were dominant, which we believe is due to the presence of surface functional groups and/or to the specifically adsorbed ionic species i.e. HSO_4^-, SO_4^{2-}, Fe^{2+}, Fe^{3+} and Cu^{2+} etc.

Pakula *et al*. [58] also demonstrated the electro-adsorption of Fe^{3+} ions on activated carbon. They concluded that with an increase in the density of oxygen containing acidic functional groups on carbon, they could significantly improve the adsorption capacity for water molecules and Fe^{3+} ions. The addition of Cu^{2+} to the electrolyte appears to catalyze the oxidation of Fe^{2+}, as proposed in the preceding discussion, which is thought to be the reason for the improved stability of the Fe^{3+} species according to reaction 7 and its adsorption on GF.

2.3 Estimating the charge storage capability by the FBFC systems

The charge storage capability of the composite electrode containing $CuFeS_2$ in the negative compartment of the FBFC system (as shown in Figure S2) was estimated using the Fe^{2+}/Fe^{3+} couple with and without the addition of Cu^{2+} ions as positive electroactive species. Figures 6a and 6b show the CV for the $CuFeS_2|Fe^{2+}$ (CFe) and $CuFeS_2|Fe^{2+}$– Cu^{2+} (CFeCu) FBFC systems, respectively, at different sweep rates (0.1 – 0.001 V s^{-1}). A higher specific current density was achieved for the CFeCu system vs. the CFe system during charging (forward) and discharging (reverse scan) cycles. The decrease in specific current density at slow sweep rate is typical behavior in the CV analysis and depends on the kinetics of the charge transfer reactions and mass transport of the electroactive species at the electrode surface. The charge transfer reactions at the high surface area GF electrode could also induce polarization effects due to the development of a concentration gradient within the porous structure of the electrode compared to the bulk

electrolyte. The continuous flow of electrolyte (7.5 ml/min) within both compartments of the FBFC ensured the continuous supply of ionic species within the porous electrode to avoid diffusion control processes by the depletion of ionic species at the surface of each electrode. Also, the conversion reactions (reduction of $CuFeS_2$ and formation of intermediate species) that occur within the negative (composite) electrode during the charging cycle affect the charging and discharging behavior of the FBFC in successive cycles. For instance, the rapid fall in specific current density with increase in sweep rate (Figure 6a & b) for both the CFe and CFeCu systems during forward and reverse cycles was due to the slow kinetics and pseudocapacitive character of the electroactive materials. In CV scans at high sweep rate, the relationship between current and cell potential indicates the limited kinetic response of the electrode materials, particularly associated with the charge transfer characteristics of the $CuFeS_2$ in the composite (negative) electrode. The mixing of carbon black (CB) (20 wt %) with the $CuFeS_2$ minimized the inter–particulate contact resistance but the formation of a sulfide sulfur enriched film on the surface of $CuFeS_2$ during the charge/discharge process likely restricts the electron transfer to or from the $CuFeS_2$. The sweep rate dependency of the Fe^{2+}/Fe^{3+} redox reaction on the GF electrode has already been discussed in the preceding section. Figure 6c shows the decrease in specific capacitance with increase in sweep rate which indicates a drop in the charge storage capability of the proposed system possibly either due to the formation of intermediate species on the surface of $CuFeS_2$ particles or by the quasi reversible nature of the redox reactions in the catholyte (Fe^{2+}/Fe^{3+} and or Cu^{2+}/Cu^{+}) as explained in section 2.2. The rapid fall in the specific capacitance at high sweep rate (Figure 6c) also confirmed the slow kinetic response of the electrode materials [59]. This behavior suggests that the current density for charging and discharging of the proposed setup, should always be lower than the maximum current density obtained in the CV scan at slow sweep rate (0.001 V s^{-1}). In this way, the maximum faradaic response of the electrode materials can be ensured in the FBFC setup. The average specific capacitance (C_{sp}) at slow sweep rate (0.001Vs^{-1}) during charging/discharging (at 1.0V cell potential) of the CFe and CFeCu systems was calculated from E1. For this system the specific capacitance was found to be 99.1 and 149.3 F g^{-1}, respectively, which decreased monotonically with increasing sweep rate as shown in Figure 6c.

$$C_{sp} = \frac{1}{msV}\int_{V_1}^{V_2} i(V).dV \qquad \text{.E1}$$

Where, 'm' is the mass (gm) of $CuFeS_2$ used in the negative electrode, 's' corresponds to the sweep rate (V s^{-1}), 'V' is the potential window (V), '$I(V)dV$' is the potential dependent current

response (A) , V_1 and V_2 correspond to initial and final potential (V), respectively. The asymmetrical cyclic current response of both systems obtained at 0.001 V s^{-1} is shown in figure 6d. This behavior was associated with the slow kinetic response of the electrode materials. The well–known refractory nature of $CuFeS_2$, its low electrical conductivity and tendency to form a passive film under acidic conditions could be the possible reasons for very low specific capacitance with increase in sweep rate.

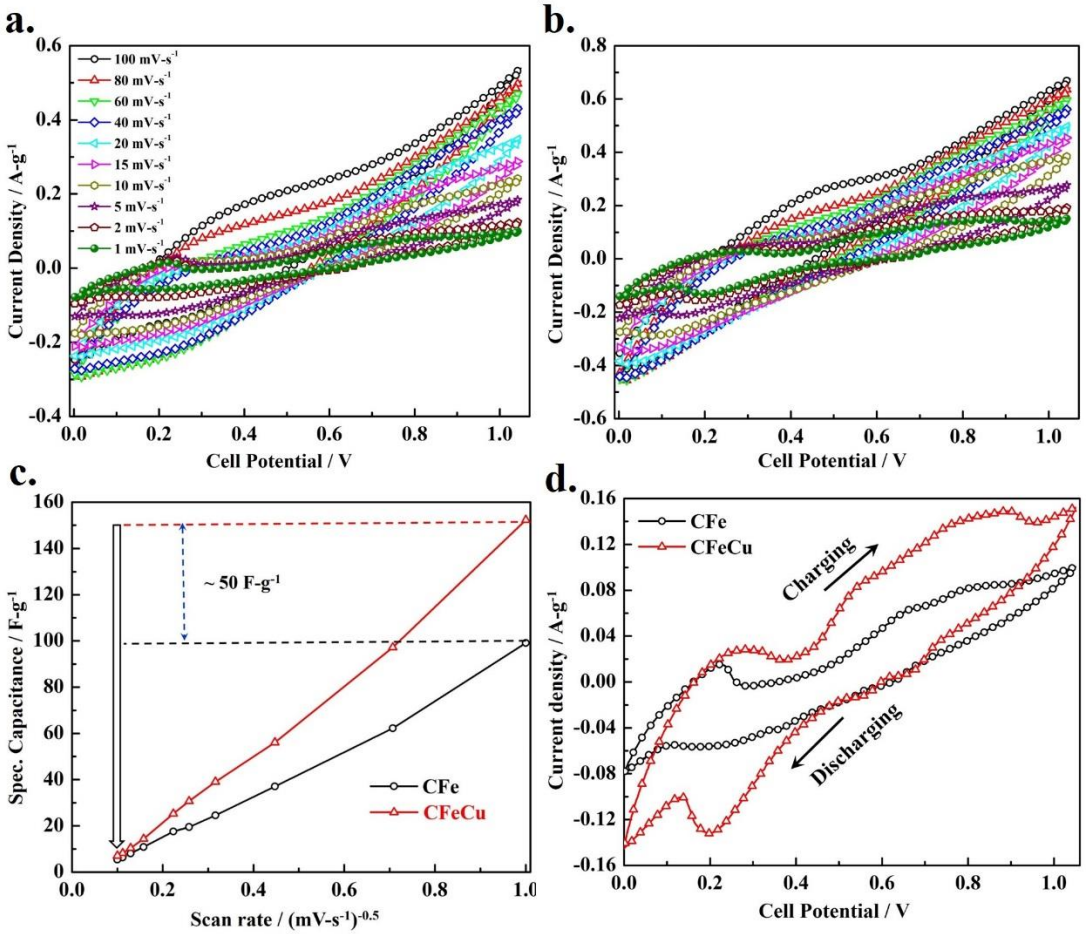

Figure 6: *CV scans for the (a) CFe and (b) CFeCu systems (c) trends showing the variation in the specific capacitance as a function of (sweep rate)$^{-0.5}$ (values obtained at 1 V cell potential), (d) comparison of charging/discharging behavior for the CFe and CFeCu system (voltammograms obtained at 1 mV s^{-1})*

In the CFe system, during the charging cycle, the oxidation reactions taking place on the positive electrodes are supported by the reduction reactions at the negative composite electrode. Similarly, the oxidation reactions on the negative electrode would occur in the following discharge cycle facilitated by the reduction of Fe^{3+} and/or Cu^{2+} on the positive electrode. It can be estimated

that for effective charge storage and retrieval, one would require high stability of Fe^{3+} ions in the catholyte. This could be achieved with the addition of Cu^{2+} in the solution as proposed in the stability analysis (*see supplementary information*). In a typical CV scan of the CFeCu system, higher anodic and cathodic current densities were observed, which were attributed to the increased stability of Fe^{3+} ions. However, based on the literature, the quasi–reversible minor redox peaks centered at about 0.55V in both the CFe and CFeCu systems represented the pseudocapacitive behavior of the GF due to the presence of surface functional groups [51].

To verify the capacitive behavior of the proposed systems and to estimate the coulombic (η_C) and energy (η_E) efficiencies of the process, GCD cyclic tests were performed from 0 to 1.05 V. The charging and discharging was carried out at 200 mA g^{-1} and 150 mA g^{-1}, respectively, and potential profiles for 500 cycles are provided for comparison in Figure 7. Analogous to the CV scans, the asymmetrical GCD plots reconfirmed the pseudocapacitive behavior of the proposed FBFC systems. A sudden potential drop of ~0.2 V at the onset of each discharge cycle was observed and may arise from the ionic resistance of the PEM, the electrolyte and/or due to the contact resistance between electrical connections. However, as noted above, the inter–particulate contact resistance in the negative composite electrode is expected to be small due to the mixing of 20 wt % conductive CB with the $CuFeS_2$. Compared to CFe, larger potential plateaus at approximately 0.2 and 0.6 V were observed in the CFeCu system during the 5^{th} GCD cycle (Figure 7a and 7b), which indicates an improvement in the electrochemical response of the FBFC due to Cu^{2+} addition in the catholyte. In the CFe system, during GCD cycling, the repetitive potential plateaus verify the occurrence of reversible redox reactions on the surface of both electrodes. In addition, the relatively lower current response of the Fe^{2+}/Fe^{3+} redox reaction (in the absence of Cu^{2+} as discussed above) resulted in short potential plateaus in the GCD curves as evident in Figure 7a. This behavior also validates the beneficial effect of Cu^{2+} addition in the catholyte and the results are in agreement with the higher current density given by the CFeCu system as shown in Figure 6d and Figure S4 (*supplementary information*). The formation of intermediate species at the GF–$CuFeS_2$ negative electrode is also possible. The enrichment of the $CuFeS_2$ surface with copper and sulfide sulfur species by the release of iron in the electrolyte under repetitive charging/discharging cycles changed the electrochemical response of the composite electrode. Sulfide species i.e. disulfide (S_2^{2-}) and bisulfide (S^{2-}) formed on the surface of $CuFeS_2$ during cyclic charging/discharging and this is seen by the potential plateau at 0.2 V.

Conway *et al.* [60] also explained the reversible pseudocapacitive character of these species over the surface of FeS_2 (pyrite) (reaction 8).

$$S_2^{2-} + 2e^- \leftrightarrow 2S^{2-} \quad .8$$

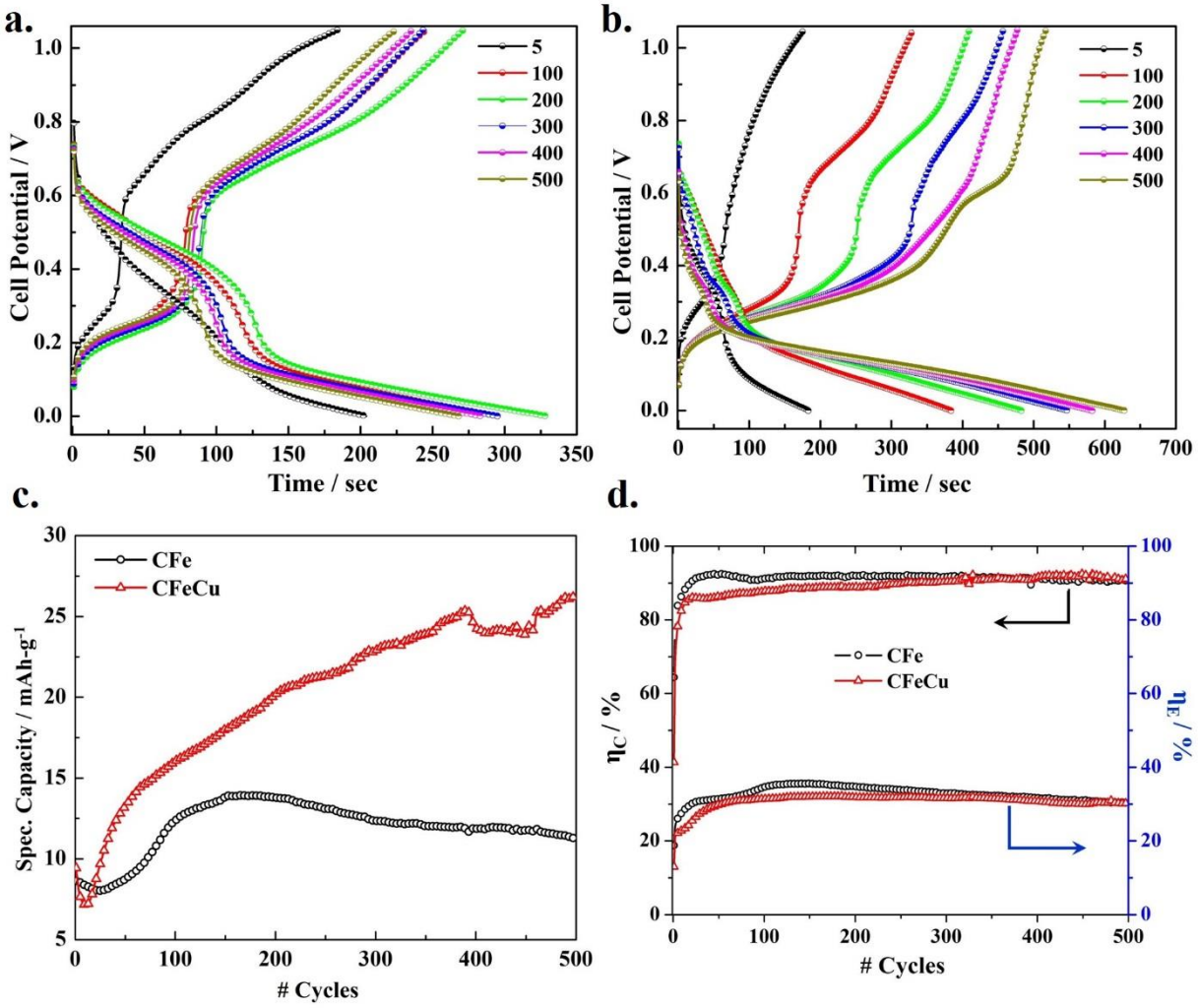

Figure 7: *Galvanostatic cyclic charge/discharge of (a) CFe and (b) CFeCu system showing the trends for 5, 100, 200, 300, 400, and 500th cycles (c) the specific capacity behavior of both systems (d) The trends showing the columbic (η_c) and energy (η_E) efficiencies of both systems as a function of number of cycles*

During the charging process, reduction of $CuFeS_2$ to talnakhite ($Cu_9Fe_8S_{16}$), bornite (Cu_5FeS_4) and/or chalcocite (Cu_2S) occurs at the negative electrode ($CuFeS_2$) [50]. These reactions are supported by the oxidation of Fe^{2+} to Fe^{3+} in the other half of the FBFC, at the positive electrode. It is also noted that during charging the potential plateaus were higher than the discharge potential for all cycles, which results from the non–capacitive faradaic reactions taking place on the surface of $CuFeS_2$. This behavior limits the reversible charge transfer processes during

repetitive charge/discharge cycles and hence deteriorates the charge storage capability of the system, as observed in the following 300 cycles.

For the CFeCu system, due to improvement in the kinetic response of the Fe^{2+}/Fe^{3+} redox reaction on the GF electrode (in the positive compartment of the FBFC) in the presence of Cu^{2+}, the span of the plateau at ~ 0.25 V was increased during continuous GCD cycling as seen in Figure 7b. These plateaus represent the concurrence of reversible redox reactions on both the electrodes and the increase in span indicates the improvement in the discharge capacity as calculated from the relation E2. The second plateau in the GCD plots also shifted to a lower cell potential, which is likely due to specific adsorption of copper species on the GF at the positive electrode. This is also corroborated by the low R_{ct} value obtained for the GF-Fe/Cu compared to GF–Fe electrode in the impedance analyses. A steep discharging profile for the CFeCu cell system is observed at higher cell potential (> 0.3 V) with a small potential plateau at approximately 0.40 V. This shorter sloping plateau could be related with the oxidation of product formed in the negative electrode during the charging process. The appearance of this plateau in the repetitive discharge cycles also indicates the reversible pseudocapacitive character of some of the intermediate species. With increase in GDC cycles, the gradual decrease in the potential below 0.25 V corresponds to an increase in charge storage capacity. The similarity in the CV and GCD profile of the CFeCu system and relatively extended discharge cycles were linked with the increased stability of Fe^{3+} ions when Cu^{2+} was present. In simple words, the Fe^{3+} ions formed in the presence of Cu^{2+} ions during charging, would be readily available during discharge and hence could increase the overall specific capacity of the system. Mai *et al.* [61] also reported an increase in specific capacitance of functionalized porous carbon with the addition of Cu^{2+} in the electrolyte. They also proposed that the reversible adsorption/desorption of Cu^{+} species with the carbonyl functional group over porous carbon could be the reason for their observed ultrahigh pseudocapacitance (4700 F g^{-1}).

The anomalous increase of the discharge specific capacity in the CFeCu system beyond 10 GCD cycles was calculated from the relation E2 and can be seen in Figure 7c. The specific capacity gradually increased to 25.4 mAh g^{-1} in 390 GCD cycles, which dropped approximately ~5% before reaching a maximum of 26.2 mAh g^{-1} in the following (up to 500 DCD) cycles. This behavior is thought to be due to the reversible character of the sulfide sulfur species present on $CuFeS_2$ (reaction 8).

$$Specific\ Capacity\ (mAh\text{-}g^{-1}) = \frac{i_d}{3.6m(V-i_dR)} \int_{t_1}^{t_2} V(t).dt \qquad .E2$$

Where 'i_d' corresponds to discharge current (A), 'V' is the overall cell potential (V), 'R' is the total cell resistance (Ω), and '$\int_{t_1}^{t_2} V(t).dt$' is the area under galvanostatic discharge profile from the start (t_1) to the end of discharge (t_2) (s), respectively.

The faradaic contribution of the Cu^{2+}/Cu^{+} redox couple in the catholyte could also facilitate the reversible pseudocapacitive response of the CFeCu system. Compared to CFeCu, the CFe system had a lower discharge capacity (13.9 mAh g^{-1}) in the initial 200 GCD cycles with a similar increasing trend. In the following 300 cycles ~18% gradual decrease in capacity was seen with this system. This fade in capacity was related to the relatively lower stability of Fe^{3+} species (within the positive electrode compartment) and its limited support for the S_2^{2-}/S^{2-} (on the negative $CuFeS_2$ electrode surface) reversible redox reaction in the cell. The existence of large polarization (relatively steep profile) and contraction in the discharging curves confirmed this behavior. Also the refractory nature of $CuFeS_2$, its passivation, and low electrical conductivity could effectively hinder the pseudocapacitive response which may ultimately deteriorate the performance of the designed cell systems. Figure 8 represents the variation in specific discharge energy during 500 GCD cycles. The specific energy of both systems was calculated from the relation E3 in which each parameter has its usual meanings. The monotonic increase in the specific energy (3.29 Wh kg^{-1}) of the CFe for the initial 150 cycles was followed by a ~30 % gradual decrease over 500 cycles. The CFeCu system had a continuous increase in specific energy over 200 cycles and plateaued (3.60 ±0.05 Wh kg^{-1}) for the successive 390 cycles. However, the atypical behavior of a sudden decrease (~10 %) and then increase of specific energy in the last 100 cycles could be related with the surface limited non–capacitive faradaic reactions (reactions 1–4 and 9–10 in the following discussion) at the $CuFeS_2$ particles in the negative composite electrode.

$$Specific\ Energy\ (Wh\ kg^{-1}) = \frac{1}{3.6m}\int_{t_1}^{t_2} \Delta V(t).i_d\,.dt \qquad \text{.E3}$$

The high coulombic efficiency (η_C) (~90%) obtained for both systems indicated the maximum utilization of charge in the capacitive faradaic reactions during charging and discharging of the system. Whereas, the low energy efficiency (η_E) (~30%) as presented in Figure 7d, suggested a large loss in specific energy during the discharge process. This loss in supplied energy was related with the cell internal resistance, IR drop and more importantly to the significant polarization effects seen in Figure 7a and b. In other words, the energy supplied to the systems during the charging process was utilized in the non-capacitive reactions specifically associated

with $CuFeS_2$ reduction into talnakhite, bornite and/or chalcocite, which might not be available during the discharge process (for the oxidation of the $CuFeS_2$ and any reaction products). To understand this behavior, the $CuFeS_2$ was retrieved from the negative electrode of the CFeCu cell (after 500 GCD cycles) and compared with the as–synthesized $CuFeS_2$.

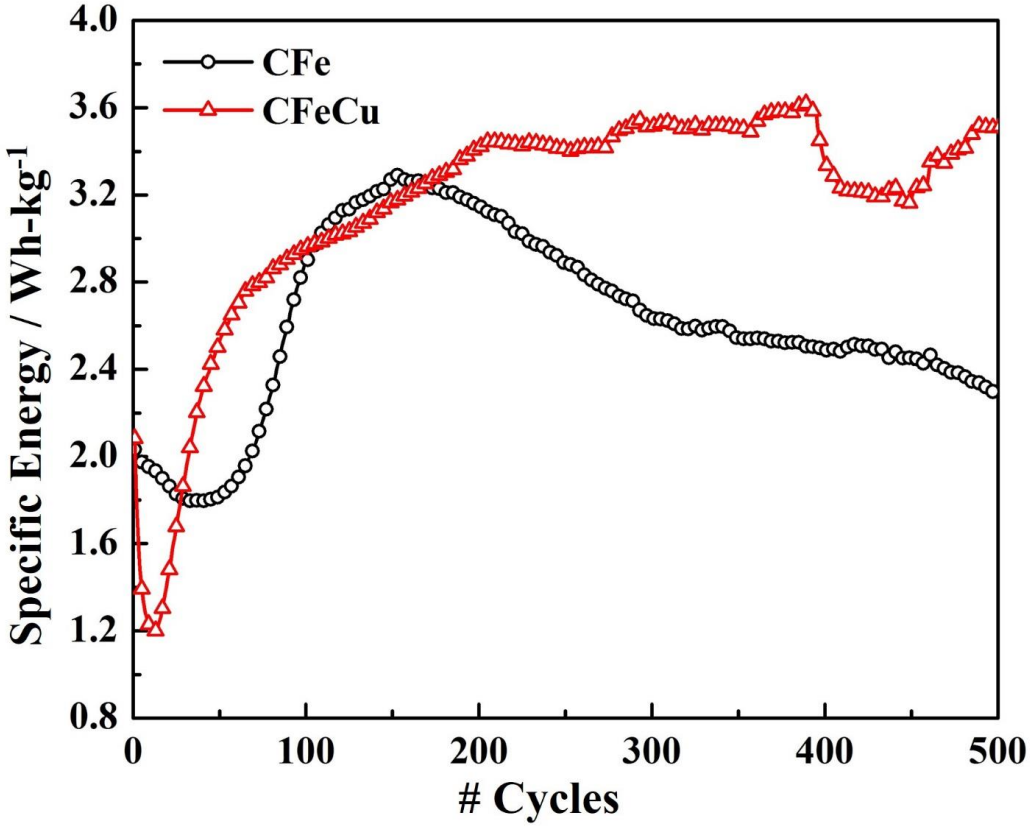

Figure 8: *Discharge specific energy profile of CFe and CFeCu system as a function of number of cycles (**Note:** Charging and discharging current density in both case was 200 mA g^{-1} and 150 mA–g^{-1}, respectively)*

2.4 Ex–Situ characterization of $CuFeS_2$

The surface morphology, composition, phase transformation and surface chemistry of the $CuFeS_2$ samples was analyzed by SEM, EDX, XRD, and XPS. It can be seen that the surface morphology of the retrieved $CuFeS_2$ samples was changed after 500 GCD cycles. The formation of a reaction product at the surface of the retrieved $CuFeS_2$ micro–spherical particles was evident as shown in Figure S7a and S7b. The EDX analysis confirmed the enrichment of copper and sulfur species in the final product after GCD cycling due to the dissolution of Fe from the surface of $CuFeS_2$ particles. The formation of copper and sulfur enriched species and depletion of iron during

reduction (herein charging) and oxidation (discharging) of $CuFeS_2$ in the acidic solution has been widely discussed in the literature [48, 62–63].

An increase in the copper content of the retrieved sample (47.8 vs. 26.3 at. %) was also detected. To probe the cause, ICP-OES was used (Varian 725–ES) to analyze both the anolyte and catholyte after cycling. A comparison of these results with the as prepared electrolytes is shown in Figure 9. It was found that during the initial 200 cycles, the concentration of Fe and Cu in the anolyte was low (0.61 and 0.03 g l^{-1}, respectively), but that it gradually increased in the remaining 300 cycles. Approximately 2.23 and 0.45 g l^{-1} of Fe and Cu, respectively, were found in the anolyte (0.2 M H_2SO_4) after 500 GCD cycles. These values include the Fe and Cu that migrated from the catholyte and leached from the $CuFeS_2$. In order to quantify the Cu dissolution from $CuFeS_2$, the loss in mass of $CuFeS_2$ was determined after 500 cycles. It was determined that ~10.75 % Cu extraction was achieved as shown in the inset of Figure 9. The dual functionality of energy storage with an additional benefit of Cu extraction by this system makes it a hybrid for both purposes. The Fe and Cu species in the anolyte could also adsorb or deposit on the composite electrode. It is for this reason that the retrieved $CuFeS_2$+CB mixture was thoroughly washed with DI water, filtered and dried in air prior to EDX and XRD analyses. Still, the presence of these species on the $CuFeS_2$ particles cannot be neglected and this may have increased the Cu contents in the retrieved product as determined by the EDX analysis (Figure S7b).

The formation of copper and sulfur enriched species were also confirmed from the XRD patterns as shown in Figure S7c. The diffraction peaks originating at 2θ values 21.2º, 31.6º, 32.5º, 33.5º, 47.8º and 52.7º correspond to the formation of CuS and Cu_9S_8 phases in the retrieved $CuFeS_2$ samples according to the 06–0464 and 36–0379 reference patterns, respectively. However, the diffraction pattern of the as synthesized sample demonstrated the characteristic peaks of pure $CuFeS_2$ which are indexed in figure 1b, in accordance with standard reference pattern (37–0471), as discussed above.

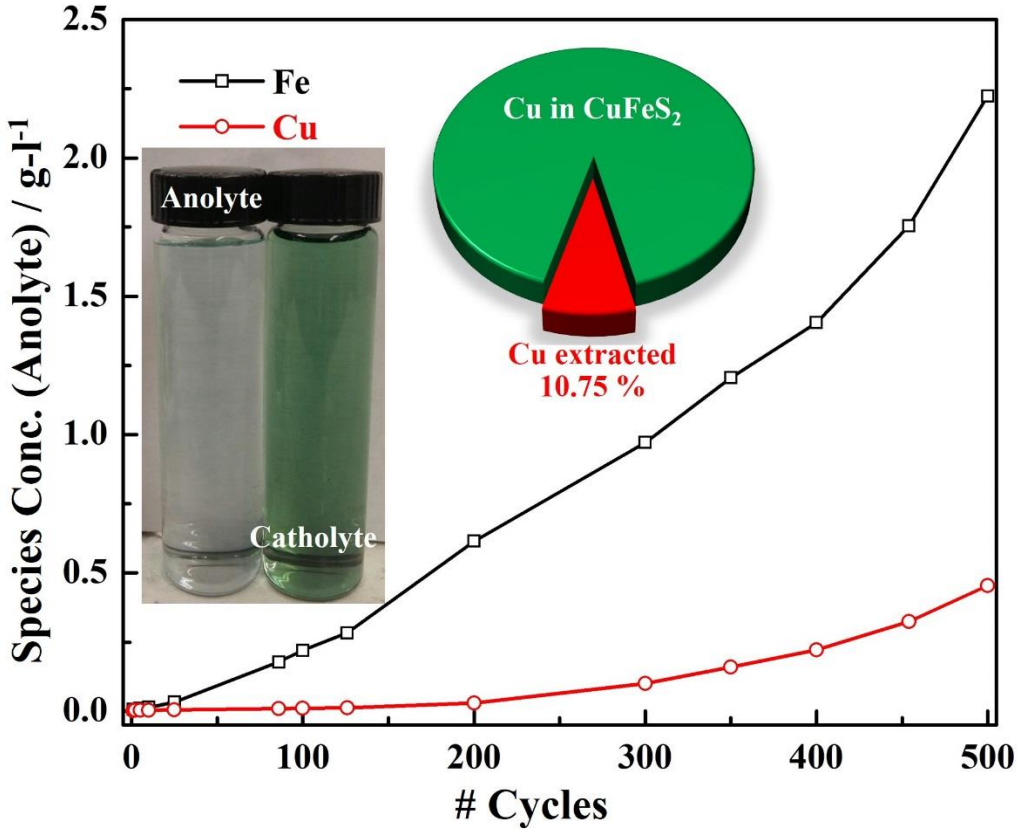

Figure 9: *The concentration of Fe and Cu species in the anolyte (migrated from catholyte + extracted from $CuFeS_2$) after 500 GCD cycles calculated from ICP-OES analysis, the inset is showing the retrieved anolyte and catholyte solutions from CFeCu cell system. % Cu extraction is also calculated from the mass loss of $CuFeS_2$ after 500 cycles (as shown in pie chart)*

The survey spectra of the as synthesized and retrieved $CuFeS_2$ were obtained on the binding energy scale. The characteristics peaks for sulfur (S) and copper (Cu) are shown in Figure 10a, b and c, respectively. The nature of the 'S' species present on the surface of $CuFeS_2$ was evaluated from the high-resolution spectra of the S 2p core peak. The deconvolution of the spectra was carried out by applying Shirley integration for background subtraction and the Gaussian-Lorentzian (80 %:20 %) function was used to split the spin orbital core S $2p_{3/2}$ peak by using Peak 4.1 software.

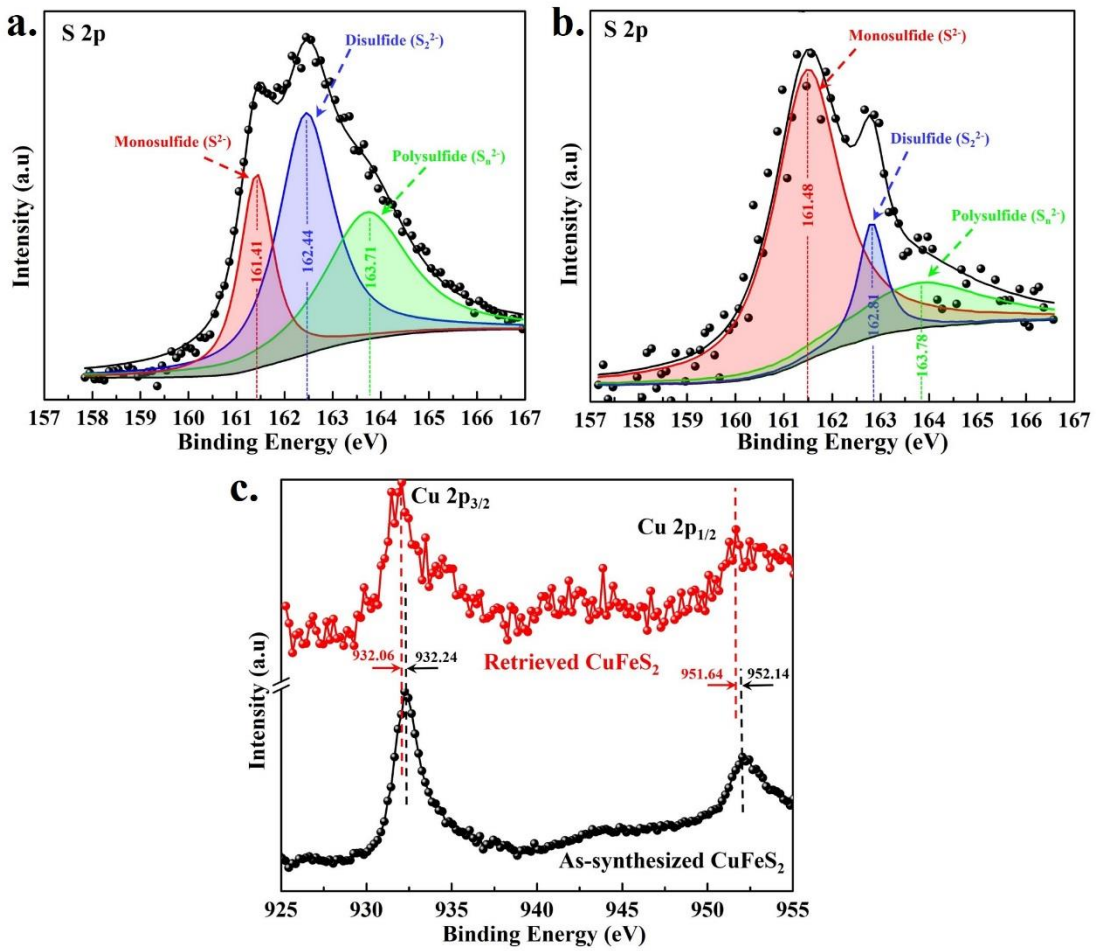

Figure 10: *X-ray photoelectron spectra of S 2p after deconvolution showing the multiple peaks related with mono, di, and poly sulfide species present over the surface of (a) as–synthesized (b) retrieved $CuFeS_2$samples from CFeCu cell system (c) doublet peaks of Cu associated with Cu $2p_{3/2}$ and Cu $2p_{1/2}$ orbital*

The deconvolution of the core S 2p peak provided the doublet S $2p_{3/2}$ peak at 161.41 and 162.44 eV, as shown in Figure 10a. The peak at the lowest binding energy (161.41 eV) validated the existence of monosulfide (S^{2-}) species at the surface of as–synthesized $CuFeS_2$ particles according to the value (161.4 eV) provided in the literature [45]. The second doublet peak at 162.44 eV was assigned to S_2^{2-}species. The 1.03 eV difference between the doublet peaks was slightly lower than the 1.1 eV reported elsewhere and corresponds to partially coordinated sulfur species at the surface [37, 64]. It is well known that the S_2^{2-} can form by the dimerization of S^{2-} species via physical relocation of sulfur atoms at the surface of $CuFeS_2$ bonded directly with the copper and/or iron atoms [65]. The relatively broad satellite peak (FWHM 1.53) observed at high binding energy

(163.71 eV) corresponds to polysulfide species (S_n^{2-}) that most likely originate from the S 3p – Fe 3d inter–band excitation [45].

Figure 10b shows the S 2p core peak for the retrieved $CuFeS_2$ sample. A clear difference in the peak distribution and change in intensity was observed after 500 GCD cycles. In the retrieved $CuFeS_2$ sample, the binding energy for the S $2p_{3/2}$ doublet peaks also shifted to higher energy values compared to the as–synthesized $CuFeS_2$. It would be reasonable to speculate from this behavior that the metal–sulfur bonding energies may change due to the formation of iron deficient species at the surface of $CuFeS_2$ during repetitive charge/discharge cycles as confirmed from the EDX and XRD analyses. Although the peak binding energy 161.48 eV (FWHM=1.63) was lower than the energy of the sulfide (S^{2-}) species in CuS (161.6 ±0.1 eV), it was dominant having 1.57 times higher peak area than shown in Figure 10a. However, the peak for the S_2^{2-} disulfide species at 162.8 eV was consistent with the literature and may be associated with covellite (CuS) [66, 67]. In addition, the broad tail peak at high binding energy 163.78 eV (FWHM=3.27) is also consistent with the existence of polysulfide species (S_n^{2-}). The relatively small energy intensity of this polysulfide species was evident, and it may decrease due to the formation of an iron deficient surface layer as it is related with the S 3p – Fe 3d inter band excitation [45]. The presence of elemental sulfur (S^o) cannot be confirmed through XPS analysis due to its volatile nature in ultra–high vacuum. Compared to as–synthesized $CuFeS_2$, the relatively higher binding energies and larger difference (1.33 eV) within the S $2p_{3/2}$ doublet peaks also suggests the formation of a metal deficient structure surface film after GCD cycling at the surface of the $CuFeS_2$ samples [41].

The XPS analysis of as–synthesized $CuFeS_2$ had core peaks at 932.24 eV and 952.14 eV, which are associated with the Cu $2p_{3/2}$ and Cu $2p_{1/2}$, respectively. However, the small variation in the binding energy after GCD cycling (retrieved sample) and the presence of a small satellite band at around 942.5 eV, is likely due to the presence of divalent copper (Cu^{2+}) species within the surface layer [46] as shown in Figure 10c. However, the decrease in binding (0.21 eV) energy of Cu 2p3/2 validated the formation of a CuS phase within the surface layer according to the binding energies (932.0 eV and 951.8) recorded by Nakai *et al.* [67]. In agreement with the EDX and XRD results, and based on the binding energy shift for both S 2p and Cu 2p species, these data are consistent with the formation of iron deficient CuS and/or Cu_9S_8 phases at the surface of $CuFeS_2$. This information is used to predict a reaction sequence that is proposed in the next section.

2.5 Proposed reaction sequence during cyclic charging/discharging process

The reactions that may proceed during charging and discharge cycles are graphically shown in Figure 11. The occurrence of non–capacitive faradaic reactions over the $CuFeS_2$ particles in the negative electrode during repetitive cycling significantly decrease the extractable energy and hence adversely affect the energy storage efficiency. One of the possible reasons for the low energy efficiency is that approximately 11 % of the Cu in the $CuFeS_2$ was dissolved. However, this is also a significant benefit to the proposed system as this Cu can be recovered hydrometallurgical for profit. The continuous increase in the specific capacity during repetitive charging and discharging cycles with high coulombic efficiency (~90%) is associated with the surface limited capacitive reversible reactions (reactions 7 and 8). During initial charging cycles, the $CuFeS_2$ is expected to transform into intermediate species i.e. talnakhite ($Cu_9Fe_8S_{16}$) and bornite (Cu_5FeS_4) before converting into chalcocite Cu_2S (reaction 2) with the generation of Fe^{2+} and $H_2S_{(aq)}$ species according to reactions 9 and 10, respectively, as pointed out by Biegler *et al*. [68] and Eghbalnia *et al*. [69].

$$9\ CuFeS_2 + 4H^+ + 2e^- \rightarrow Cu_9Fe_8S_{16} + 2H_2S + Fe^{2+} \quad .9$$

$$5CuFeS_2 + 12\ H+ + 4e^- \rightarrow Cu_5FeS_4 + 6H_2S + 4Fe^{2+} \quad .10$$

A very low pH is required for these reactions to move in the forward direction during the charging process. In order to estimate the in–situ pH change in the $CuFeS_2$ slurry and to support the proposed mechanism, we performed a few experiments in the two-electrode setup shown in Figure S8. The progress of these reactions can be judged from the pH variation results as discussed separately in the *supplementary information*.

These non–capacitive conversion reactions likely consume a large amount of supplied energy during the initial charging cycles, which is consistent with the low specific capacity and specific energy measurements, η_c and η_E, respectively.

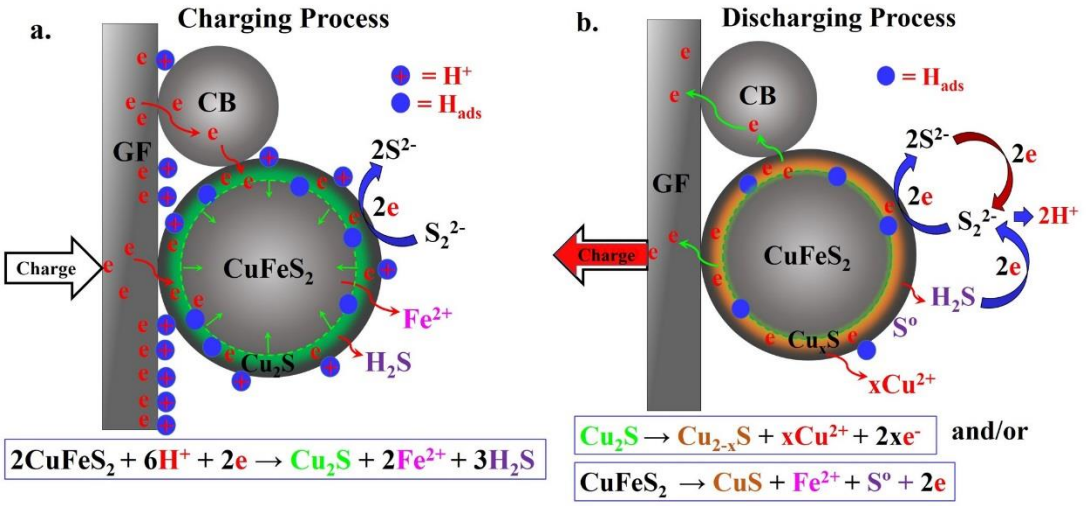

Figure 11: *Schematic diagram showing the proposed reactions sequence occurring on negative electrode in the FBFC system during (a) charging and (b) discharging process*

It is proposed that during discharging, any unreacted $CuFeS_2$ is oxidized into metal depleted sulfide $Cu_{1-x}Fe_{1-y}S_{2-z}$ (reaction 1) or can convert into CuS. In the repetitive charging and discharging cycles the reduction of $CuFeS_2$ and oxidation of chalcocite (Cu_2S) into a series of products i.e. djurleite ($Cu_{1.92}S$), degenite ($Cu_{1.60}S$) and covellite (CuS), is also possible (reaction 5) [52, 70].

The generation of $H_2S_{(aq)}$ during the charging process can oxidize into either elemental sulfur (S^o) or to the disulfide (S_2^{2-}) species by a non–oxidative dissolution mechanism (reaction 6 and 11, respectively) [70, 71]. These reactions were found to be reversible and enhanced the capacitive faradaic response as evident from the increased specific capacity and energy of the CFeCu system. Furthermore, the reversible transformation of S_2^{2-} into S^{2-} (reaction 8) during cyclic GCD is also possible as discussed above.

$$2H_2S_{(aq)} = 4H^+ + S_2^{2-} + 2e^- \quad .11$$

During continuous GCD cycling of the CFeCu cell setup, the generation of Fe^{2+} and Cu^{2+} species by the dissolution of $CuFeS_2$ in the negative electrode (or that diffused from the positive half of the cell) have been verified through ICP analysis. These species are beneficial to enhance the overall specific capacity and energy of the system. These species may react reversibly with the surface products formed at the $CuFeS_2$/electrolyte interface, e.g. CuS, S^o and/or $H_2S_{(aq)}$ according to reactions 6, 12, 13 and 14, respectively [72, 73].

$$CuS + Cu^{2+} + 2e^- = Cu_2S \quad .12$$

$$S^o + Cu^{2+} + 2e^- = CuS \quad .13$$

$H_2S + 2Cu^{2+} + 2e^- = Cu_2S + 2H^+$ .14

The literature also indicates that the addition of Cu^{2+} ions to the acidic solution could also facilitate the reduction of $CuFeS_2$ into Cu_5FeS_4 and/or Cu_2S (reactions 15 and 16) [74].

$2CuFeS_2 + 3Cu^{2+} + 4e^- = Cu_5FeS_4 + Fe^{2+}$ .15

$CuFeS_2 + 3Cu^{2+} + 4e^- = 2Cu_2S + Fe^{2+}$ .16

The formation of iron deficient species at the surface of $CuFeS_2$, and their reversible character (reactions 8, 12–14) has augmented the cyclic performance of the proposed system as evident from the continuous increase in specific capacity and energy during repetitive GCD cycling. However, the large amount of energy supplied during charging was utilized in the conversion reactions e.g. Cu extraction, which adversely affected the energy storage capacity and efficiency of the proposed systems. In other words, the non–capacitive faradaic reactions e.g. 10.75 % dissolution of Cu from $CuFeS_2$ would consume energy during charge/discharge cycles. Although, the maximum specific energy provided by this system is low compared to the commercially available energy storage systems, the Cu recovery from $CuFeS_2$ provides an additional benefit that may be monetized.

3. Conclusion

The use of synthetic $CuFeS_2$ as the negative electrode material in a laboratory designed FBFC system is presented. This hybrid system has the dual capability of storing energy at the $CuFeS_2$ surface and extracting Cu from the $CuFeS_2$. The reduction of $CuFeS_2$ to Cu_2S and oxidation of the latter species, or any unreacted $CuFeS_2$, to CuS/Cu^{2+} was supported by the Fe^{2+}/Fe^{3+} redox reaction during the charge/discharge process in this hybrid system. The main conclusions of this study are:

1. $CuFeS_2$ oxidation or reduction is sluggish (0.2M H_2SO_4). On the other hand, the Fe^{2+}/Fe^{3+} redox reaction is rapid on the GF (positive) electrode.
2. The addition of 0.1M Cu^{2+} in the catholyte increased the current response of the Fe^{2+}/Fe^{3+} redox reaction, which was shown to be due to the increased stability of the Fe^{3+} ionic species and catalytic behavior of Cu^{2+} towards Fe^{2+} oxidation over the GF electrode. This increased the specific current density of the CFeCu system during charging and discharging processes as predicted form the CV scans at 0.001 V s^{-1}.
3. The specific capacity of the CFeCu systems increased continuously to 26.2 mAh g^{-1} during 500 GCD cycles having a coulombic efficiency over ~90%. The CFe system, on the other

hand, provided a relatively low capacity of 13.9 mAh g^{-1} in the initial 150 cycles followed by an 18% gradual decrease in the next 350 cycles.

4. The energy storage capability of the CFeCu increased gradually to 3.60±0.05 from 1.2 Wh–kg^{-1} in 500 GCD cycles but the energy efficiency remained low at 30 %. However, in the CFe system, the specific energy reached a maximum of 3.29 Wh kg^{-1} in the initial 150 cycles and decreased 30% in the successive 350 cycles.
5. The cause of limited energy storage and low energy efficiency in this system (CFeCu) was also identified from the ex-situ analysis of the retrieved product. The energy consumed during charging of the CFeCu system was due to the non–capacitive conversion reactions on the $CuFeS_2$ surface such as dissolution of Cu from $CuFeS_2$. While these reactions limit the energy storage of this system, they provide a source of copper that could be readily recovered.

It is clear that the addition of Fe^{2+} and Cu^{2+} in the anolyte improves the energy storage capability of the CFeCu system. The reversible character of these species, i.e. reduction of Cu^{2+} and oxidation of Fe^{2+}, on the surface of $CuFeS_2$ during charging and discharging processes, respectively, enhances both the energy storage and Cu extraction capabilities of this system. Copper could be recovered from the process using standard hydrometallurgical methods including solid/liquid separation and solvent extraction followed by Cu electrowinning.

The flow of $CuFeS_2$ in the form of slurry in this hybrid setup would be more useful for continuous supply of energy and Cu extraction without the depletion of active mass ($CuFeS_2$) in the cell. Ultimately, natural $CuFeS_2$ mineral concentrates (instead of synthetic $CuFeS_2$) will be tried in this hybrid system and reports on this are forthcoming.

4. Experimental

The synthesis of chalcopyrite ($CuFeS_2$) is described elsewhere [34]. Briefly, stoichiometric amounts of lab grade cupric chloride di-hydrate ($CuCl_2.2H_2O$), ferrous chloride tetra-hydrate ($FeCl_2.4H_2O$) (99.95%, Fisher Scientific) and thiourea ($CS(NH_2)_2$) (99.98%, Alfa Aesar) were mixed homogeneously in 150ml of deionized water. The mixture was heated for 12 h at 200ºC in a sealed, Teflon-lined, steel vessel by placing it in a furnace. The product was rinsed in DI water and 2% (v/v) sulfuric acid solution followed by washing in DI water to remove any soluble impurities. The filtered product was dried in an oven at 50 ºC for 24 h before further use.

To investigate the surface morphology of $CuFeS_2$, Scanning Electron Microscopy (Hitachi S3000N VP–SEM) images were obtained. Energy dispersive X–ray (EDX) analysis was also carried out to evaluate any variation in the elemental composition of $CuFeS_2$ particles before and after galvanostatic charging/discharging (GCD). The X-ray diffraction (XRD) patterns were obtained with a Rigaku MultiFlex X-ray diffractometer using a Cu Kα1 radiation source (λ = 0.15405 nm). The X-rays were generated at 40 kV and a filament current of 20 mA in a vacuum tube. The diffraction patterns were analyzed by Jade 6 (Materials Data Inc.) software. The Kα2 signals and background noise were removed before analyzing the XRD patterns.

The average size and surface area of the $CuFeS_2$ particles was measured by laser diffraction (Malvern Mastersizer Hydro 2000S) and the multipoint Brunauer–Emmett–Teller (BET) (Quantachrome Autosorb-1) method, respectively. The pore size distribution and average pore volume was calculated from the N_2 adsorption/desorption isotherm (77.5K) and by using density functional theory (DFT) calculations. The out gassing of the powder samples was done at 25 ºC for 20.5 h in a 6 mm glass bulb before isothermal analysis.

Time of Flight Secondary Ion Mass Spectroscopy (ToF-SIMS) (TRIFT V nano TOF; Physical Electronics) was used to determine the surface characteristics of as-synthesized $CuFeS_2$ particles. Briefly, the sample powder was mounted on a commercially available (1 cm^2) silicon wafer by using double sided adhesive tape. Both positive and negative mass spectra were collected by pulsing a 30 keV Au* primary ion beam over a 400 µm X 400 µm raster area with a total ion dose < 10^{12} ions/cm^2. In the acquisition of spectral data and images, high mass and spatial resolution was achieved by applying the bunched and un-bunched mode, respectively. To investigate the variation in the surface composition of $CuFeS_2$ particles before and after CD cycling, X-ray Photoelectron Spectroscopy (XPS) (Leybold MAX2000 spectrometer) analyses were carried out. A Mg Kα (1253.6 eV) X-ray beam was used and the emitted photo-electrons were analyzed at 90º take off angle in a hemispherical energy analyzer. The characteristic high resolution spectra of 'Cu', 'Fe' and 'S' core peaks were analyzed on the binding energy scale with the XPS peak 4.1 software. Shirley background subtraction and a Gaussian (80 %) – Lorentzian (20 %) function was applied to resolve the fractional spectra of the S $2p_{3/2}$ core peaks, particularly. No sputtering or charge neutralization were performed and any peak shifting was identified with respect to the C 1s adventitious peak.

The electrochemical behavior of a given electrode used in the final FBFC was investigated in its respective electrolyte as detailed in Table S1 (*supplementary information*). The anode (negative) was a composite of graphite felt (GFE-1, CeraMaterials) (GF) and as–synthesized $CuFeS_2$ particles (80 wt. %) mixed with carbon black (CB) (20 wt. %). The composite electrode was prepared by sandwiching $CuFeS_2$ particles manually within the two halves of the GF. The edges of the GF were sealed with carbon paste (Carbon black (CB) +poly (vinyl di-fluoride); PVDF (4:1)). This composite electrode was then connected to a solid graphite rod with the same carbon paste to complete the working electrode assembly. The cathode (positive electrode) was made of only GF and connected similarly with a graphite rod. Potentiodynamic polarization (PD) scans, linear scan voltammetry, cyclic voltammetry (CV) and electrochemical impedance spectroscopy (EIS) analyses were done to characterize the electrochemical response of the electrode materials and to estimate their performance in the actual FBFC system. (*Note:* the designation of the electrode system given here is based on the polarity of electrodes in the *FBFC* during the discharge cycle).

Electrochemical testing of individual electrode systems was carried out in a water jacketed cell to maintain a constant temperature (25 ± 1.0 ºC) throughout the experiment, as shown in Figure S1. A graphite rod and a mercury/mercury (I) sulfate (Hg/Hg_2SO_4) (0.620mV vs. SHE) electrode were used as counter and reference electrodes, respectively. Prior to each experiment, deaeration of the electrolytes was done by N_2 gas sparging for 30 min. A Gamry Reference-600 potentiostat was used to conduct all the electrochemical tests. All the potential values in this study are reported with respect to the standard hydrogen electrode (SHE) unless otherwise stated. Details about the experimental input parameters can be found in the *supplementary file (section S–Experimental).*

The design of the FBFC used in this study is shown in Figure S2. The construction, experimental conditions and details on the preparation of electrodes is also provided in *supplementary information.* Under optimized conditions, the performance of the proposed FBFC system was evaluated by cyclic voltammetry (CV) and cyclic galvanostatic charging/discharging (GCD). In order to identify the electrochemical behavior and maximum current response of the FBFC system, the CV scans were obtained at various sweep rates ($0.1Vs^{-1}$ – $0.001Vs^{-1}$). The specific capacity, energy density, coulombic efficiency, energy efficiency and cyclic performance of the FBFC system was calculated from the cyclic GCD profile.

The possible reaction mechanism during GCD performance was evaluated by post-experimental analyses of retrieved $CuFeS_2$ from the composite electrode. The surface morphology, phase transformation and any change in the surface composition of the retrieved samples was analyzed and compared through SEM, EDS, XRD and XPS.

Further details on the experimental procedure for electrochemical analyses of the individual electrodes and for the FBFC setup is provided in the supplementary file (*S – Experimental*).

Acknowledgement

The first author acknowledges partial funding from the University of the Punjab, Lahore, Pakistan to pursue further education. The financial support by The University of British Columbia and the Natural Sciences and Engineering Research Council of Canada (NSERC) is also gratefully acknowledged.

References

[1] A. S. Arico, P. Bruce, B. Scrosati, J. M. Tarascon, W. V. Schalkwijk, *Nat. Mater*., 4 (2005), 366–377

[2] P. Simon, Y. Gogotsi, *Nat. Mater*., 7 (2008) 845–854

[3] C. Liu, F. Li, L. P. Ma, H. M. Cheng, *Adv. Mater*., 22 (2010) E28–E62

[4] Z. Q. Niu, L. Zhang, L. Liu, B. W. Zhu, H. B. Dong, X. D. Chen, *Adv. Mater*., 25 (2013) 4035–4042

[5] Z. Q. Niu, P. S. Luan, Q. Shao, H. B. Dong, J. Z. Li, J. Chen, D. Zhao, L. Cai, W. Y. Zhou, X. D. Chen, S. S. Xie, *Energy Environ. Sci*., 5 (2012) 8726–8733

[6] X. C. Dong, Y. F. Cao, J. Wang, M. B. Chan-Park, L. H. Wang, W. Huang, P. Chen, *RSC Adv*., 2 (2012) 4364–4369

[7] B. Kang, G. Ceder, *Nat. Letters*. 458 (2009) 190-193

[8] Z. Hu, Z. Zhu, F. Cheng, K. Zhang, J. Wang, C. Chen, J. Chen, *Energy Environ. Sci.*, 8 (2015) 1309-1316

[9] X. Wu, Y. Zhao, C. Yang, G. He, *J. Mater Sci.* 50 (2015) 4250-4257

[10] W. Ding, X. Wang, H. Peng, L. Hu, *Mat. Chem. Phy*., 137 (2013) 872-876

[11] N. Eda, T. Fujii, H. Koshina, A. Morita, H. Ogawa, K. M. Murakami, *J. Power Sources*, 20 (1987) 119-126

[12] J.W. Marple, High energy capacity Lithium battery, Patent US 7,968,230 B2 (2011)

[13] Y. S. Horn, Q. C. Horn, *Electrochimica Acta*, 46 (2001) 2613–2621

[14] D. Dreisinger, Hydrometallurgy 83 (2006) 10-29

[15] E. Peters, Met. Trans. B, 7B (1976) 505-517

[16] D.L. Jones, The leaching of chalcopyrite, PhD. Thesis, Department of Metals and Materials Engineering, University of British Columbia, Vancouver, Canada, 1974

[17] Y. J. Xian, S. M. Wen, J. S. Deng, J. Liu, Q. Nie, Cana. Metal. Quart.,51(2) (2012) 133-140

[18] J. E. Dutrizac. Hydrometallurgy, 29 (1992)1–45

[19] H.G. Linge, Hydrometallurgy, 2 (1977), pp. 219–233

[20] Q. Yin, G.H. Kelsall, D.J. Vaughan, K.E.R. England, Geochim. Cosmochim. Acta, 59 (1995), 1091–1100

[21] C. Klauber, A. Parker, W. van Bronswijk, H. Watling, Int. J. Miner. Proc., 62 (2001), 65–94

[22] A.J. Parker, R.L. Paul, G.P. Power, J. Electroanal. Chem. Interf. Electrochem, 118 (1981) 305–316

[23] A. Ghahremaninezhad, D. G. Dixon, E. Asselin, Electrochim. Acta, 87 (2013) 97-112

[24] R. P. Hackl, D. B. Dreisinger, E. Peters, J. A. King, Hydrometallurgy, 39 (1995) 25-48

[25] (a) F. K. Crundwell, Cana. Metal. Quart, 54 (2015) 279–288. (b) L.J.Bryson, A. V. Aswegen, B. Knights, F. K. Crundwell, Hydrometallurgy Conference Proceedings (2016) 173–183

[26] (a) M. J. Nicol, Hydrometallurgy 169 (2017) 99–102. (b) M. J. Nicol, Hydrometallurgy 163 (2016) 104–107

[27] (a) P. R. Holmes, F. K. Crundwell, Hydrometallurgy 139 (2013) 101–110. (b) F. K. Crundwell, A.V. Aswegen, L. J. Bryson, C. Biley, D. Craig, V. D. Marsicano, J. M. Keartland, Hydrometallurgy 158 (2015) 119–131. (c) M. J. Nicol, S. Zhang, Hydrometallurgy 167 (2017) 72–80. (d) M. J. Nicol, Hydrometallurgy 169 (2017) 321–329. (e) A. Ghahremaninezhad, R. Redzinski, T. Gheorghiu, D. G. Dixon, E. Asselin, Hydrometallurgy 155 (2015) 95–104

[28] B. E. Conway, J.C.H. Ku, F. C. Ho, FeS_2, J. Coll. Interf. Sci., 75 (2) (1980) 357-372

[29] G. Hasegawa, M. Aoki, K. Kanamori, K. Nakanishi, T. Hanada, K. Tadanaga, J. Mater. Chem., 21 (2011) 2060

[30] Y. Huang, S. L. Candelaria, Y. Li, Z. Li, J. Tian, L. Zhang, G. Cao, J. Power Sour., 252 (2014) 90-97

[31] K. Yang, L. Peng, D. Shu, C. Lv, C. He, L. Long, J. Power Sources, 239 (2013) 553-560

[32] Y. Yang, L. Liu, Y. Tang, Y. Zhang, D. Jia, L. Kong, Electrochimica Acta, doi:10.1016/j.electacta.2016.01.149

[33] G. Yue, E. Asselin, Electrochimica Acta 146 (2014) 307-321

[34] R.M. Garrels, C.L. Christ, Solution, Minerals, and Equilibria, Harper & Row, New York (1965), p. 231

[35] E.M. Córdoba, J.A. Muñoz, M.L. Blázquez, F. González, A. Ballester, Hydrometallurgy 93 (2008) 81–87

[36] A. Ghahremaninezhad, D.G. Dixon, E. Asselin, Hydrometallurgy 125–126 (2012) 42–49

[37] K. M. Deen, E. Asselin, Electrochimica Acta, 212 (2016) 979–991

[38] G. Halsey, J. Chem. Phys., 16 (1948) 931 – 937

[39] K. Sing, Colloids and surfaces A; Physico chem. Eng. Aspects 3–9 (2001) 187–188

[40] M. A. Harahsheh, S. Kingman, F. Rutten, D. Briggs, Int. J. Min. Process., 80 (2-4) (2006) 205–214

[41] A.N. Buckley, R. Woods, Aus. J. Chem., 37 (1984) 2403 – 2413

[42] Y. Li, N. Kawashima, J. Li, A. P. Chandra, A. R. Gerson, Adv. Colloid Inter. Sci., 197–198 (2013) 1–32

[43] O.G. Olvera, M. Rebeolledo, E. Asselin, Hydrometallurgy 165 (2016) 148 – 158

[44] J. N. Soderberg, A. C. Co, A. H. C. Sirk, V. I. Birss, J. Phys. Chem. B 110 (2006) 10401–10410

[45] A. Ghahremaninezhad, D.G. Dixon, E. Asselin, Electrochimica Acta, 87 (2013) 97 – 112

[46] R. P. Hackl, D. B. Dreisinger, E. Peters, J.A. King, Hydrometallurgy, 39 (1995) 25–48

[47] D. Nava, I. Gonzalez, Electrochimica Acta (2006) 5295-5303

[48] J.C. Fuentes-Aceituno, G.T. Lapidus, F.M. Doyle, Hydrometallurgy 92 (2008) 26–33

[49] (a) J. Ye, P. C. Chiu, Environ. Sci. Technol., 40 (2006) 3959–3964 (b) F. H. Yang, R. T. Yang, Carbon, 40 (2002) 437–444

[50] D. Nava, I. Gonzalez, D. Leinen, J. R. R. Barrado, Electrochimica Acta, 53 (2008) 4889 – 4899

[51] H. A. Andreas, B. E. Conway, Electrochimica Acta, 51 (2006) 6510–6520

[52] E. M. Arce, I. Gonzalez, Int. J. Miner. Process 67 (2002) 17 – 28

[53] K. F. Blurton, Electrochimica Acta, 18 (1973) 869–875

[54] G. Senanayake, Hydrometallurgy, 98 (2009) 21–32

[55] A. E. Elsherief, Miner. Engineering, 15 (2002) 215–223

[56] G. A. Mabbott, J. Chem. Edu., 60 (1983) 697–702

[57] M. G–Cuenca, W. Zipprich, B. A. Boukamp, G. Pudmich, F. Tietz, Fuel Cells, 1 (3–4) (2001) 256–264

[58] M. Pakula, S. Biniak, A. Swiatkowski, Langmuir 24 (1998) 3082–3089

[59] A. Singh, A. Chandra, Sci. Rep. 5 (2015) 15551

[60] B.E. Conway, J. C. H. Ku. F. C. Ho, 75 (1980) 357–372

[61] L.Q. Mai, A. M. Khan, X. Tian, K. M. Hercule, Y.L. Zhao, X. Lin, X. Xu, Nat. Commun., 4 (2013) 2923– 2929

[62] G. W. Warren, H. J. Sohn, M. E. Wadsworth, T. G. Wang, Hydrometallurgy, 14 (1985) 133–149

[63] R. I. Holliday, W.R. Richmond, J. Electroanal. Chem. 288 (1990) 83–98

[64] C. Klauber, A. Parker, W. V. Bronswijik, H. Watling, Int. J. Min. Process., 62 (2001) 65–94

[65] C. Klauber, Surf. Interface. Anal., 35 (2003) 415–428

[66] H.B. Zhao, M. H Hu, Y.N. Li, S. Zhu, W. Q. Qin, G.Z. Qiu, J. Wang, Trans. Nonferrous Met. Soc. China 25 (2015) 303−313

[67] I. Nakai, Y. Sugitani, K. Nagashima, J. Inorg. Nucl. Chem., 40 (1978) 789-791

[68] T. Biegler, D.A. Swift, J. Appl. Electrochem., 6 (3) (1976) 229–235

[69] M. Eghbalnia, D. G. Dixon, Hydrometallurgy 110 (2011) 1–12

[70] H. B. Zhao, M. H. Hu, Y.N. Li, S. Zhu, W.Q. Qin, G. Z. Qin, J. Wang, Trans. Nonferrous Met. Soc. China 25 (2015) 303 – 313

[71] Y. Li, N. Kawashima, J. li, A.P. Chandra, A. R. Gerson, Adv. Colloid Inter. Sci., 197–198 (2013) 1–32

[72] J. Gerlach, E. Kuzeci, Hydrometallurgy, 11 (1983) 345–361

[73] C. Gomez, M. Figueroa, J. Munoz, M. L. Blazquez, A. Ballester, Hydrometallurgy 43 (1996) 331–344

[74] A.E. Elsherief, Minerals Engineering, 15 (2002) 215-223